Advances in Nano Research, *Vol. 18, No. 3 (2025) 223-239*
https://doi.org/10.12989/anr.2025.18.3.223

Novel methodology to mitigate vibrations in nanocomposites reinforced smart systems rested on concrete auxetic foundation by artificial intelligence algorithm

Hao Li*[1], Cheng Zhang[2], Yudong Han[1], Tong Zhang[1] and Ameni Brahmia[3]

[1]*School of Civil Engineering, University of Science and Technology Liaoning, Anshan, 114051, China*
[2]*Liaoning Metallurgical Geological Exploration Research Institute Co, Anshan, 114038, China*
[3]*Department of Chemistry, College of Science, King Khalid University, P.O. Box 9004, 61413 Abha, Saudi Arabia*

(*Received November 14, 2024, Revised February 24, 2025, Accepted February 26, 2025*)

Abstract. This study presents a novel methodology for mitigating vibrations in sandwich plates with sensor/actuator face sheets and a carbon nanotube (CNT)-reinforced core, resting on a concrete auxetic foundation under external loading. A comprehensive mathematical simulation framework is developed, incorporating higher-order shear deformation theory and Hamilton's principle to model the dynamic behavior of the system. The proposed approach integrates an artificial intelligence-based deep neural network (DNN) to enhance accuracy and validate the numerical results. The sensor/actuator face sheets, equipped with piezoelectric layers, enable active control of vibrations through real-time feedback mechanisms, while the CNT-reinforced core enhances stiffness and damping characteristics. The unique auxetic properties of the concrete foundation further contribute to energy dissipation and vibration reduction. The study systematically examines the effects of CNT distribution, auxetic parameters, and control strategies on the dynamic response of the sandwich plate. The mathematical model is trained using high-fidelity datasets, and the DNN algorithm optimizes predictive accuracy, demonstrating superior agreement with benchmark numerical solutions. Results confirm the efficacy of the proposed methodology in reducing vibrations, offering significant improvements over conventional passive and active control techniques. The developed framework provides valuable insights for designing intelligent structural systems with enhanced vibration suppression capabilities, contributing to the advancement of high-performance aerospace, civil, and mechanical engineering applications. Future research directions include experimental validation and extending the approach to nonlinear dynamic regimes.
Keywords: carbon nanotube reinforcement; concrete auxetic foundation; deep neural networks; sandwich plate; vibration mitigation

1. Introduction

Nanocomposites have emerged as a crucial advancement in engineering due to their superior mechanical, thermal, and electrical properties compared to conventional materials (Azmi *et al*. 2019). Their incorporation into structural components enhances strength-to-weight ratios, making them highly desirable for aerospace, automotive, and civil engineering applications (Ebrahimi *et al*. 2019). The inclusion of nanoparticles, such as carbon nanotubes and graphene, significantly improves stiffness, toughness, and durability, allowing engineers to design more efficient and resilient structures (Ebrahimi *et al*. 2019). Additionally, nanocomposites exhibit enhanced thermal stability and corrosion resistance, which are essential for improving the longevity of engineering systems operating in harsh environments (Hajmohammad *et al*. 2018). Their unique electrical and piezoelectric properties enable the development of smart materials with self-sensing and self-healing capabilities, revolutionizing fields such as structural health monitoring and adaptive materials (Jayakumari *et al*. 2024). Engineers also benefit from nanocomposites' improved energy absorption and damping characteristics, which are critical for vibration control and impact resistance in mechanical and aerospace structures (Madenci *et al*. 2023). Furthermore, their lightweight nature reduces fuel consumption in transportation applications, contributing to energy efficiency and sustainability (Moradi *et al*. 2022). The versatility of nanocomposites allows for multifunctional applications, integrating mechanical reinforcement with electrical conductivity and thermal management in advanced engineering designs (Xia *et al*. 2023). With the rapid progress in nanotechnology, engineers can now tailor nanocomposite properties at the molecular level, optimizing performance for specific applications (Ye *et al*. 2024). As research continues, nanocomposites are expected to play a pivotal role in the development of next-generation materials, enabling innovative engineering solutions across multiple industries (Zerrouki *et al*. 2020).

Stability analysis is a critical aspect of structural engineering, ensuring that various structures can withstand external forces without experiencing failure (Bentrar *et al*. 2023, Beitollahi *et al*. 2025). Engineers must assess structural stability to prevent catastrophic collapses that could result in significant economic losses and human casualties (Gawah *et al*. 2025). The study of stability involves evaluating the response of structures under different loading conditions, including static, dynamic, and

*Corresponding author, Ph.D.,
E-mail: lh13904180780@163.com

ISSN: 2287-237X (Print), 2287-2388 (Online)

environmental loads (Gawah *et al*. 2024). Vibrational analysis is a key component of stability assessments, particularly for slender structures such as columns, beams, and shells, where instability can occur due to compressive forces (Youzera *et al*. 2025). Engineers utilize mathematical modeling and computational methods, such as the finite element method (FEM), to predict stability behavior and optimize structural designs (Al-Houri *et al*. 2024). Stability analysis is crucial for high-rise buildings, bridges, aircraft, and offshore structures, where safety and durability are paramount (Tounsi *et al*. 2024). The effects of geometric imperfections, material properties, and boundary conditions must be carefully considered to ensure the reliability of engineering structures (Belabed *et al*. 2024). In addition to traditional methods, advanced techniques such as artificial intelligence and machine learning are increasingly being integrated into stability analysis for improved accuracy and efficiency (Belabed *et al*. 2024a). Real-time monitoring systems equipped with sensors allow engineers to track stability parameters and detect potential failures before they become critical (Al-Houri *et al*. 2024). Stability assessments also play a vital role in earthquake-resistant design, where structures must withstand seismic forces without excessive deformation or collapse (Zerrouki *et al*. 2024). Engineers must evaluate both linear and nonlinear stability phenomena to account for complex structural behaviors under varying loads (Alsubaie *et al*. 2024). The design of sustainable and cost-effective structures relies on rigorous stability analysis to optimize material usage while maintaining safety standards (Boutaleb *et al*. 2024). Furthermore, understanding the interaction between structural components and environmental factors, such as wind and temperature fluctuations, is essential for long-term performance (Cuong *et al*. 2024). Stability considerations are also crucial in aerospace and mechanical engineering, where lightweight materials and innovative designs must be balanced with safety requirements (Alsubaie *et al*. 2023). Recent advancements in computational simulations and optimization techniques have enhanced the precision and reliability of stability predictions (Mangalasseri *et al*. 2023). Engineers are now able to incorporate probabilistic and risk-based approaches to assess the likelihood of instability under uncertain conditions (Zhang *et al*. 2023). The integration of smart materials and adaptive structures has further expanded the possibilities of enhancing stability in modern engineering applications (Huang *et al*. 2021). As engineering challenges become more complex, stability analysis remains a fundamental tool for ensuring the structural integrity of both conventional and cutting-edge designs (Belabed *et al*. 2024b). The continuous development of stability assessment methodologies enables engineers to create resilient and efficient structures, meeting the growing demands of infrastructure and technology (Belabed *et al*. 2024c). Through multidisciplinary collaboration, stability analysis will continue to evolve, addressing the challenges of modern engineering and enhancing the safety and functionality of future structures (Lakhdar *et al*. 2024).

Machine learning algorithms have become essential predictive tools for engineers, enabling accurate forecasting and optimization in complex engineering systems (Samaniego *et al*. 2020). These algorithms can analyze vast datasets, identify hidden patterns, and improve decision-making in structural analysis, material design, and system monitoring (Zhuang *et al*. 2021). Engineers utilize machine learning for predictive maintenance, reducing downtime and enhancing the lifespan of critical infrastructure (Guo 2021). In civil engineering, machine learning models improve structural health monitoring by detecting early signs of damage and preventing catastrophic failures (Ahmed *et al*. 2023). Similarly, in mechanical and aerospace engineering, these algorithms optimize performance by predicting material behavior, fatigue life, and dynamic responses under varying conditions (Mortazavi *et al*. 2023). The integration of artificial intelligence enhances automation in design processes, reducing computational costs and improving efficiency (He *et al*. 2022). Advanced deep learning techniques further refine engineering simulations by providing highly accurate approximations of nonlinear and complex physical behaviors (Goswami *et al*. 2020). The adaptability of machine learning allows engineers to optimize control systems, energy consumption, and safety mechanisms across various industries (Buaria and Sreenivasan 2023). Moreover, the continuous advancement in algorithmic learning capabilities ensures that predictive models evolve with new data, improving their accuracy over time (Li *et al*. 2023). As engineering challenges become increasingly complex, machine learning remains a transformative tool, revolutionizing predictive analytics and intelligent decision-making (Wu *et al*. 2024). Computer simulation plays a crucial role in modern engineering by enabling precise modeling, analysis, and optimization of complex systems (Gong and Li 2024, Yang *et al*. 2024). It allows engineers to replicate real-world phenomena in a virtual environment, reducing the need for costly physical prototypes (Su *et al*. 2022, Yang *et al*. 2024). By leveraging numerical methods and computational algorithms, simulations provide insights into structural behavior, fluid dynamics, thermal responses, and electromagnetic interactions (Shu *et al*. 2025, Wang *et al*. 2025). These tools help engineers predict performance, identify weaknesses, and enhance design efficiency (Bibi *et al*. 2024, Wang *et al*. 2024). Simulation facilitates rapid testing of multiple design iterations, accelerating product development cycles while minimizing material waste (Zhou *et al*. 2022, Long *et al*. 2024). It enables engineers to assess system reliability under various operational conditions without the risks associated with physical testing (Song *et al*. 2024, Xu *et al*. 2025). In aerospace and automotive industries, simulation is essential for analyzing aerodynamic forces and crashworthiness (Huang *et al*. 2021, Zhang *et al*. 2022). In civil engineering, it supports structural integrity assessments and earthquake-resistant design (Huang *et al*. 2021, Guo *et al*. 2022). Biomechanical simulations contribute to medical device innovation and human body modeling for healthcare applications (Yang *et al*. 2023, Zhang *et al*. 2024). Moreover, computer simulation enhances decision-making by integrating real-time data and artificial intelligence-based predictive models (Chen *et al*. 2023, Song *et al*. 2024). The ability to simulate extreme conditions, such as high-temperature environments or high-

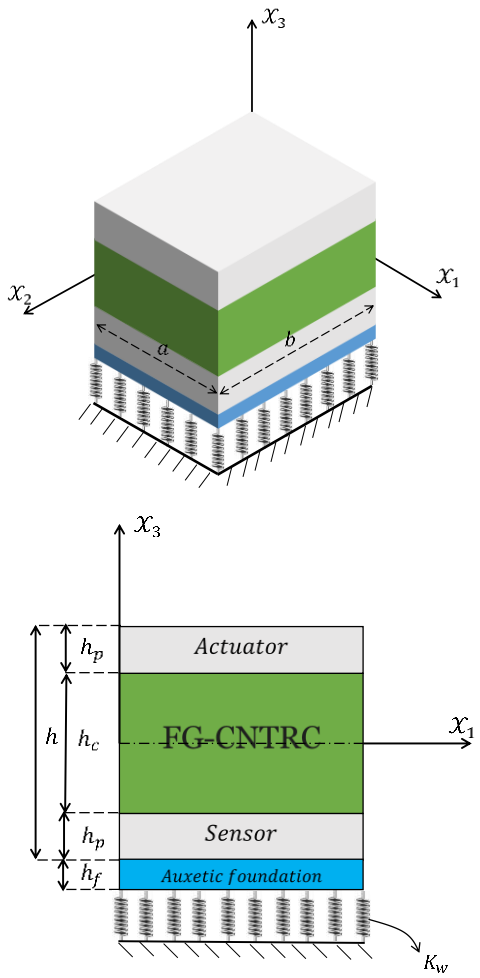

Fig. 1 Schematic representation of a sandwich plate

$(a) FG-UD$ $(b) FG-X$ $(c)\ FG-O$

Fig. 2 Distribution patterns of CNTs in thickness of the presented plate

speed impacts, is invaluable in safety-critical applications (Yang *et al*. 2023, 2024). Engineers also use multiphysics simulations to analyze interactions between mechanical, thermal, and electrical phenomena in complex systems (Hu *et al*. 2023, Yang *et al*. 2024). Additionally, digital twins—virtual replicas of physical assets—enhance monitoring, predictive maintenance, and lifecycle management (Han *et al*. 2023, Wu *et al*. 2023). The growing use of high-performance computing and cloud-based simulation platforms has further expanded engineering capabilities (Taheri *et al*. 2021, Han *et al*. 2023). These advancements enable large-scale simulations with higher accuracy and computational efficiency (Taheri *et al*. 2020, Liu *et al*. 2021). With increasing environmental and sustainability concerns, simulation aids in optimizing energy consumption, reducing emissions, and developing eco-friendly materials (Feng *et al*. 2021, Firouzianhaji *et al*. 2021). Ultimately, computer simulation enhances engineering innovation, improves safety, and drives cost-effective solutions across industries (Taheri *et al*. 2019, Mehrabi *et al*. 2021). In civil engineering, it supports structural integrity assessments and earthquake-resistant design (Toghroli *et al*. 2020, Mehrabi *et al*. 2021). Moreover, computer simulation enhances decision-making by integrating real-time data and artificial intelligence-based predictive models (Mehrabi *et al*. 2024, Mehrabi *et al*. 2025).

For the first time, this research proposed an advanced methodology for mitigating vibrations in sandwich plates with sensor/actuator face sheets and a carbon nanotube-reinforced core, supported by a concrete auxetic foundation under external loading. A mathematical model based on higher-order shear deformation theory and Hamilton's principle was developed to analyze the dynamic response of the system. To enhance accuracy and validation, a deep neural network was employed as an artificial intelligence algorithm, ensuring reliable numerical predictions. The study investigated the combined effects of CNT reinforcement, piezoelectric face sheets, and auxetic foundation properties on vibration suppression. The results demonstrated that CNT distribution patterns significantly influenced the stiffness and damping characteristics of the sandwich plate, while the piezoelectric layers provided an active control mechanism to counteract external disturbances. Furthermore, the auxetic foundation played a crucial role in reducing vibrations due to its negative Poisson's ratio, which improved energy absorption and redistribution. The proposed AI-assisted framework exhibited high predictive accuracy, validating the mathematical model and offering a robust tool for intelligent structural analysis. Parametric studies confirmed that optimizing material properties and control mechanisms enhanced the system's vibration mitigation performance. The findings highlighted the effectiveness of integrating advanced materials, active control strategies, and artificial intelligence in designing high-performance structures. This research contributed to the development of intelligent vibration control techniques for aerospace, mechanical, and civil engineering applications. Future work should extend the approach to nonlinear dynamic behaviors and experimental validation to further refine the proposed methodology.

2. Theory and Formulation

The free vibration analysis of a functionally graded CNT-reinforced plate encased by two identical piezoelectric layers is detailed as follows. Fig. 1 also presents a schematic representation of the structure.

The distribution of the reinforcements, referred to as CNTs, may be accomplished in two manners: uniformly ($FG-UD$) or functionally graded with two distinct patterns, $FG-X$ and $FG-O$. The distributions are shown in Fig. 2.

2.1 Properties of composite media

The microstructure comprises an isotropic matrix combined with single-walled carbon nanotubes (CNTs). The

dispersion of through-thickness CNTs, shown in Fig. 4, includes a uniform distribution ($FG-UD$) as well as FG distributions designated as $FG-X$ and $FG-O$. In $FG-O$, the mid-plane has a high concentration of CNT, but in $FG-X$, both the top and bottom surfaces are abundant in CNT. The volume fraction of nanotubes is expressed in Eq. (1).

$$V_{CNT}(\mathcal{X}_3)=\begin{cases} V^*_{CNT} & FG-UD \\ 2\left(1-\dfrac{2|\mathcal{X}_3|}{h_c}\right)V^*_{CNT} & FG-O \\ 4\left(\dfrac{|\mathcal{X}_3|}{h_c}\right)V^*_{CNT} & FG-X \end{cases} \tag{1}$$

V^*_{CNT} is obtained using Eq. (2).

$$V^*_{CNT}=\frac{W_{CNT}}{W_{CNT}+(\frac{\rho^{CNT}}{\rho^m})-(\frac{\rho^{CNT}}{\rho^m})W_{CNT}} \tag{2}$$

where W_{CNT} shows CNT mass fraction while ρ^m, ρ^{CNT} are matrix and CNT densities, respectively.

$$E_{11}=\eta_1 V_{CNT}E^{CNT}_{11}+V_mE^m,$$

$$\frac{\eta_2}{E_{22}}=\frac{V_{CNT}}{E^{CNT}_{22}}+\frac{V_m}{E^m},$$

$$\frac{\eta_3}{G_{12}}=\frac{V_{CNT}}{G^{CNT}_{12}}+\frac{V_m}{G^m},$$

$$\begin{gathered}\nu_{12}=\nu^{CNT}_{12}V_{CNT}+\nu_mV_m=\nu^{CNT}_{12}V_{CNT}+\nu_m(1-\\ V_{CNT})=\nu_m+(\nu^{CNT}_{12}-\nu_m)V_{CNT},\end{gathered} \tag{3}$$

$$\nu_{21}=\nu_{12}E_{22}/E_{11},$$

$$\begin{gathered}\rho=\rho_{CNT}V_{CNT}+\rho_mV_m=\rho_{CNT}V_{CNT}+\rho_m(1-\\ V_{CNT})=\rho_m+(\rho_{CNT}-\rho_m)V_{CNT},\end{gathered}$$

$$\begin{gathered}E_{33}=E_{22},G_{12}=G_{13}=G_{23},\nu_{13}=\nu_{12},\nu_{31}=\\ \nu_{21},\nu_{32}=\nu_{23}=\nu_{21},\end{gathered}$$

E_{11} and E_{22} represent the effective elastic moduli, G_{12} denotes the shear modulus, ν_{12} and ν_{21} indicate Poisson's ratios, and ρ signifies mass density. "CNT" denotes carbon nanotube qualities, whereas "m" refers to matrix material properties. The volume fraction of the matrix will be determined using the Eq. $V_m=1-V_{CNT}$. Moreover, $\eta_j(j=1,2,3)$ is an efficiency measure related to size effects and the contribution of load applied to nanotubes and polymeric phases. The characteristics of the used materials are detailed in Ref. (Mirzaei and Kiani 2016).

3. Mathematic model derivation

Various theories may be used to estimate and simulate the displacement in beams, plates, and shells, as referenced in (Nazemizadeh *et al*. 2020). A higher-order theory using a hyperbolic function known as Mechab theory is used to determine the displacement field of the sandwich plate. The displacement function of the sandwich plate is then derived as follows (Ansari *et al*. 2018):

$$\begin{gathered}\mathbb{U}_1(\mathcal{X}_1,\mathcal{X}_2,\mathcal{X}_3,t)=\mathbb{u}_0(\mathcal{X}_1,\mathcal{X}_2,t)+\\ f(\mathcal{X}_3)\mathbb{u}_1(\mathcal{X}_1,\mathcal{X}_2,t)+g(\mathcal{X}_3)\mathbb{w}_{0,\mathcal{X}_1}(\mathcal{X}_1,\mathcal{X}_2,t),\end{gathered}$$

$$\begin{gathered}\mathbb{U}_2(\mathcal{X}_1,\mathcal{X}_2,\mathcal{X}_3,t)=\mathbb{v}_0(\mathcal{X}_1,\mathcal{X}_2,t)+\\ f(\mathcal{X}_3)\mathbb{v}_1(\mathcal{X}_1,\mathcal{X}_2,t)+g(\mathcal{X}_3)\mathbb{w}_{0,\mathcal{X}_2}(\mathcal{X}_1,\mathcal{X}_2,t),\end{gathered} \tag{4}$$

$$\mathbb{U}_3(\mathcal{X}_1,\mathcal{X}_2,\mathcal{X}_3,t)=\mathbb{w}_0(\mathcal{X}_1,\mathcal{X}_2,t).$$

The displacements on the mid-plane along the $\mathcal{X}_1$-, $\mathcal{X}_2$- and $\mathcal{X}_3$-axes are denoted by $\mathbb{u}_0$, $\mathbb{v}_0$ and $\mathbb{w}_0$, respectively. Furthermore, $\mathbb{u}_1$ and $\mathbb{v}_1$ denote the rotations of the transverse normal around the $\mathcal{X}_2$ - and $\mathcal{X}_1$ -axes, respectively.

$f(\mathcal{X}_3)$, and $g(\mathcal{X}_3)$, the hyperbolic functions used in Mechab theory (Ait Atmane, Tounsi, Mechab *et al*. 2010), are articulated in Eq. (5). It is noteworthy that $\mathbb{u}_0$, $\mathbb{v}_0$, and $\mathbb{w}_0$ are designated as mid-plane displacements in the $\mathcal{X}_1$, $\mathcal{X}_2$, and $\mathcal{X}_3$ directions.

$$\begin{gathered}f(\mathcal{X}_3)=\frac{cosh(\pi/2)}{cosh(\pi/2)-1}\mathcal{X}_3-\frac{\mathrm{h}/\pi}{cosh(\pi/2)-1}sinh(\pi\mathcal{X}_3/h),\\ g(\mathcal{X}_3)=f(\mathcal{X}_3)-\mathcal{X}_3.\end{gathered} \tag{5}$$

Based on the provided displacement field, linear strain-displacement relationships for in-plane strains may be articulated as follows.

$$\begin{gathered}\mathcal{E}_{11}=\mathbb{U}_{1,\mathcal{X}_1}=\mathrm{E}^0_{11}+\mathcal{X}_3\kappa_1=\mathbb{u}_{0,\mathcal{X}_1}+\\ f(\mathcal{X}_3)\mathbb{u}_{1,\mathcal{X}_1}+g(\mathcal{X}_3)\mathbb{w}_{0,\mathcal{X}_1\mathcal{X}_1},\end{gathered}$$

$$\begin{gathered}\mathcal{E}_{22}=\mathbb{U}_{2,\mathcal{X}_2}=\mathrm{E}^0_{22}+\mathcal{X}_3\kappa_1=\mathbb{v}_{0,\mathcal{X}_1}+\\ f(\mathcal{X}_3)\mathbb{v}_{1,\mathcal{X}_2}+g(\mathcal{X}_3)\mathbb{w}_{0,\mathcal{X}_2\mathcal{X}_2},\end{gathered}$$

$$\begin{gathered}\mathcal{E}_{12}=\mathbb{U}_{1,\mathcal{X}_2}+\mathbb{U}_{2,\mathcal{X}_1}=\mathrm{E}^0_{12}+\mathcal{X}_3\kappa_{12}=\mathbb{u}_{0,\mathcal{X}_2}+\\ \mathbb{v}_{0,\mathcal{X}_1}+f(\mathcal{X}_3)\left(\mathbb{u}_{1,\mathcal{X}_2}+\mathbb{v}_{1,\mathcal{X}_1}\right)+g(\mathcal{X}_3)\left(\mathbb{w}_{0,\mathcal{X}_1\mathcal{X}_2}+\right.\\ \left.\mathbb{w}_{0,\mathcal{X}_2\mathcal{X}_1}\right),\end{gathered} \tag{6}$$

$$\begin{gathered}\mathcal{E}_{23}=\mathcal{E}^0_{23}=f'(\mathcal{X}_3)\mathbb{v}_1(\mathcal{X}_1,\mathcal{X}_2,t)+g'(\mathcal{X}_3)\mathbb{w}_{0,\mathcal{X}_2}+\\ \mathbb{w}_{0,\mathcal{X}_2},\end{gathered}$$

$$\begin{gathered}\mathcal{E}_{13}=\mathcal{E}^0_{13}=f'(\mathcal{X}_3)\mathbb{u}_1(\mathcal{X}_1,\mathcal{X}_2,t)+\\ g'(\mathcal{X}_3)\mathbb{w}_{0,\mathcal{X}_1}+\mathbb{w}_{0,\mathcal{X}_1}.\end{gathered}$$

In above relations and hereafter, (,) stands for differential operator.

4. Constitutive relations

4.1 Constitutive relations of CNTRC layers

For CNTRC layers, Hooke's rule, consistent with the constraint of σ^c_{33} being zero, indicates that the stress vector is represented as $\sigma^c=[\sigma^c_{11},\sigma^c_{22},\sigma^c_{12},\sigma^c_{13},\sigma^c_{23}]^T$. The stress tensor and strain vector, $\boldsymbol{\mathcal{E}}=[\mathcal{E}_{11}.\mathcal{E}_{22},2\mathcal{E}_{12},2\mathcal{E}_{13},2\mathcal{E}_{23}]^T$ are interconnected by the following relation:

$$\boldsymbol{\sigma}^c=\mathbf{C}^c\boldsymbol{\mathcal{E}}, \tag{7}$$

$\mathbf{C}^c$ is the elastic constant matrix for the CNTRC layer.

$$\mathbf{C}^c = \begin{bmatrix} \mathbf{C}_1^c & 0 \\ 0 & \mathbf{C}_2^c \end{bmatrix},$$
$$\mathbf{C}_1^c = \begin{bmatrix} \frac{E_{11}}{1-\nu_{12}\nu_{21}} & \frac{\nu_{21}E_{11}}{1-\nu_{12}\nu_{21}} & 0 \\ \frac{\nu_{21}E_{11}}{1-\nu_{12}\nu_{21}} & \frac{E_{22}}{1-\nu_{12}\nu_{21}} & 0 \\ 0 & 0 & G_{12} \end{bmatrix}, \quad (8)$$
$$\mathbf{C}_2^c = \begin{bmatrix} G_{13} & 0 \\ 0 & G_{23} \end{bmatrix}.$$

where, k_w and Ψ are constant and VEF parameters. Note that if Ψ is zero, the EF becomes uniform.

4.2 Constitutive relations of top and bottom piezoelectric layers

According to the theory of piezoelasticity, the constitutive relationship of piezoelectric layers may be expressed as:

$$\begin{Bmatrix} \boldsymbol{\sigma}^{\boldsymbol{p}} \\ \boldsymbol{D} \end{Bmatrix} = \begin{bmatrix} \mathbf{C}^{\mathbf{p}} & -\mathbf{e}^T \\ \mathbf{e} & \Xi \end{bmatrix} \begin{Bmatrix} \boldsymbol{\mathcal{E}} \\ \boldsymbol{E} \end{Bmatrix} \quad (9)$$

In Eq. (9), $\mathbf{C}^{\mathbf{p}}$ denotes the elastic constant matrix for the piezoelectric layers, $\mathbf{E}$ represents the dielectric permittivity constant matrix, and $\mathbf{e}$ indicates the electromechanical coupling matrix, hence, they possess the following definitions:

$$\mathbf{C}^{\mathbf{p}} = \begin{bmatrix} \overline{Q}_{11}^p & \overline{Q}_{12}^p & 0 & 0 & 0 \\ \overline{Q}_{12}^p & \overline{Q}_{22}^p & 0 & 0 & 0 \\ 0 & 0 & \overline{Q}_{66}^p & 0 & 0 \\ 0 & 0 & 0 & Q_{44}^p & 0 \\ 0 & 0 & 0 & 0 & Q_{55}^p \end{bmatrix},$$
$$\mathbf{e} = \begin{bmatrix} 0 & 0 & 0 & e_{15} & 0 \\ 0 & 0 & e_{15} & 0 & 0 \\ \overline{e}_{31} & \overline{e}_{31} & 0 & 0 & 0 \end{bmatrix}, \quad (10)$$
$$\Xi = \begin{bmatrix} \Xi_{11} & 0 & 0 \\ 0 & \Xi_{22} & 0 \\ 0 & 0 & \overline{\Xi}_{33} \end{bmatrix}.$$

Elastic matrix components related to piezoelectric material are presented as

$$\overline{Q}_{11}^p = \overline{Q}_{22}^p = Q_{11}^p - \frac{Q_{13}^p Q_{13}^p}{Q_{33}^p},$$
$$\overline{Q}_{12}^p = Q_{12}^p - \frac{Q_{13}^p Q_{13}^p}{Q_{33}^p},$$
$$\overline{Q}_{66}^p = \frac{1}{2}\left(\overline{Q}_{11}^p - \overline{Q}_{12}^p\right), \quad (11)$$
$$\overline{e}_{31} = e_{31} - \frac{Q_{13}^p}{Q_{33}^p} e_{33},$$
$$\overline{\Xi}_{33} = \Xi_{33} + \frac{e_{33}^2}{Q_{33}^p}.$$

Furthermore, $\boldsymbol{\sigma}^{\boldsymbol{p}}$, $\mathbf{E}$ and $\mathbf{D}$ denote the stress field in piezoelectric layers adhering to the condition of null σ_{33}^p, the electric field, and the electric displacement field, respectively, and may be expressed as:

$$\boldsymbol{\sigma}^{\mathrm{p}} = \left[\sigma_{11}^p, \sigma_{22}^p, \sigma_{12}^p, \sigma_{23}^p, \sigma_{13}^p\right]^T,$$
$$\mathbf{D} = [D_1, D_2, D_3]^T, \quad (12)$$
$$\mathbf{E} = [E_1, E_2, E_3]^T = -\left[\Phi_{,\mathcal{X}_1}, \Phi_{,\mathcal{X}_2}, \Phi_{,\mathcal{X}_3}\right]^T.$$

where Φ is the electrical potential function, which will be defined in line with the electrical boundary conditions thereafter. The comparatively thin piezoelectric layers justify the assumption of linearity in the variations of electric potential over their thickness. The electrical potential function in the upper and lower piezoelectric layers may be expressed as:

$$\Phi(\mathcal{X}_1, \mathcal{X}_2, \mathcal{X}_3) = \begin{cases} -cos\left(\pi\left(\frac{2\mathcal{X}_3 - h_c - h_p}{2h_p}\right)\right)\psi_a(\mathcal{X}_1, \mathcal{X}_2) 0.5h_c < 0.5h_c + h_p \\ -cos\left(\pi\left(\frac{2\mathcal{X}_3 + h_c + h_p}{2h_p}\right)\right)\psi_s(\mathcal{X}_1, \mathcal{X}_2) - 0.5h_c - h_p < z < -0.5h_c \end{cases} \quad (13)$$

In the aforementioned connection, it is assumed that the surfaces of the piezoelectric layers next to the CNTRC layers are grounded, hence, the electrical potential at these surfaces is zero.

The governing Eq.s are derived by using Hamilton's principle, which is expanded in the following manner for the situation under study (Reddy 2003):

$$\int_0^t (\delta\mathbb{U} - (\delta T + \delta W_1 + \delta W_2 + \delta W_3))\,\mathrm{d}t = 0 \quad (14)$$

where t represents an arbitrary point in time. The fluctuations in strain energy, $\delta\mathbb{U}$, and kinetic energy, δT, for the sandwich plate are computed as follows:

$$\begin{aligned} \delta\mathbb{U} = & \int_{-0.5b}^{0.5b} \int_{-0.5a}^{0.5a} \int_{-0.5h_c}^{0.5h_c} \{\sigma_{11}^c \delta\mathcal{E}_{11} + \sigma_{22}^c \delta\mathcal{E}_{22} + 2\sigma_{12}^c \delta\mathcal{E}_{12} + 2\sigma_{23}^c \delta\mathcal{E}_{23} + 2\sigma_{13}^c \delta\mathcal{E}_{13}\} \mathrm{d}\mathcal{X}_3 \mathrm{d}\mathcal{X}_1 \mathrm{d}\mathcal{X}_2 + \\ & \int_{-0.5b}^{0.5b} \int_{-0.5a}^{0.5a} \int_{0.5h_c}^{0.5h_c+0.5h_p} \{\sigma_{11}^p \delta\mathcal{E}_{11} + \sigma_{22}^p \delta\mathcal{E}_{22} + 2\sigma_{12}^p \delta\mathcal{E}_{12} + 2\sigma_{23}^p \delta\mathcal{E}_{23} + 2\sigma_{13}^p \delta\mathcal{E}_{13} - D_1\delta E_1 - D_2\delta E_2 - D_3\delta E_3\} \mathrm{d}\mathcal{X}_3 \mathrm{d}\mathcal{X}_1 \mathrm{d}\mathcal{X}_2 + \\ & \int_{-0.5b}^{0.5b} \int_{-0.5a}^{0.5a} \int_{-0.5h_c-0.5h_p}^{-0.5h_c} \{\sigma_{11}^p \delta\mathcal{E}_{11} + \sigma_{22}^p \delta\mathcal{E}_{22} + 2\sigma_{12}^p \delta\mathcal{E}_{12} + 2\sigma_{23}^p \delta\mathcal{E}_{23} + 2\sigma_{13}^p \delta\mathcal{E}_{13} - D_1\delta E_1 - D_2\delta E_2 - D_3\delta E_3) \mathrm{d}\mathcal{X}_3 \mathrm{d}\mathcal{X}_1 \mathrm{d}\mathcal{X}_2\}, \end{aligned} \quad (15a)$$

$$\begin{aligned} \delta T = & \int_{-0.5b}^{0.5b} \int_{-0.5a}^{0.5a} \int_{-0.5h_c}^{0.5h_c} \left\{\rho^{(k)}\left\{\dot{\mathbb{U}}_1\left[\delta\dot{\mathrm{u}}_0 + f(\mathcal{X}_3)\delta\dot{\mathrm{u}}_1 + g(\mathcal{X}_3)\delta\dot{\mathrm{w}}_{0,\mathcal{X}_1}\right] + \dot{\mathbb{U}}_2\left[\delta\dot{\mathrm{v}}_0 + f(\mathcal{X}_3)\delta\dot{\mathrm{v}}_1 + g(\mathcal{X}_3)\delta\dot{\mathrm{w}}_{0,\mathcal{X}_2}\right] + \dot{\mathbb{U}}_3\delta\dot{\mathrm{w}}_0\right\}\right\} \mathrm{d}\mathcal{X}_3 \mathrm{d}\mathcal{X}_1 \mathrm{d}\mathcal{X}_2 + \\ & \int_{-0.5b}^{0.5b} \int_{-0.5a}^{0.5a} \int_{0.5h_c}^{0.5h_c+0.5h_p} \left\{\rho^{p}\left\{\dot{\mathbb{U}}_1\left[\delta\dot{\mathrm{u}}_0 + f(\mathcal{X}_3)\delta\dot{\mathrm{u}}_1 + g(\mathcal{X}_3)\delta\dot{\mathrm{w}}_{0,\mathcal{X}_1}\right] + \dot{\mathbb{U}}_2\left[\delta\dot{\mathrm{v}}_0 + f(\mathcal{X}_3)\delta\dot{\mathrm{v}}_1 + g(\mathcal{X}_3)\delta\dot{\mathrm{w}}_{0,\mathcal{X}_2}\right] + \dot{\mathbb{U}}_3\delta\dot{\mathrm{w}}_0\right\}\right\} \mathrm{d}\mathcal{X}_3 \mathrm{d}\mathcal{X}_1 \mathrm{d}\mathcal{X}_2 + \end{aligned} \quad (15b)$$

$$\int_{-0.5b}^{0.5b}\int_{-0.5a}^{0.5a}\int_{-0.5h_c-0.5h_p}^{-0.5h_c}\Big\{\rho^p\big\{\dot{\mathbb{U}}_1[\delta\dot{\mathbb{u}}_0+f(\mathcal{X}_3)\delta\dot{\mathbb{u}}_1+g(\mathcal{X}_3)\delta\dot{\mathbb{w}}_{0,\mathcal{X}_1}]+\dot{\mathbb{U}}_2[\delta\dot{\mathbb{v}}_0+f(\mathcal{X}_3)\delta\dot{\mathbb{v}}_1+g(\mathcal{X}_3)\delta\dot{\mathbb{w}}_{0,\mathcal{X}_2}]+\dot{\mathbb{U}}_3\delta\dot{\mathbb{w}}_0\big\}\Big\}\mathrm{d}\mathcal{X}_3\mathrm{d}\mathcal{X}_1\mathrm{d}\mathcal{X}_2,$$

The following mathematical formula pertains to a Haber-Schaim foundation composed of auxetic material inside the Cartesian coordinate system (Behravan-Rad and Jafari 2020):

$$\delta W_1=\int_A\left(K_w\mathbb{w}+D_f\nabla^4\mathbb{w}\right)\delta\mathbb{w}dA. \tag{16}$$

The Winkler coefficient, foundation plate thickness, and Poisson's ratio of the auxetic foundation are represented by the symbols K_w, ν_f, and h_f, respectively. D_f is comparable to $\frac{E_f{h_f}^3}{12(1-\nu_f^2)}$. The virtual work of a transverse distributed external force, $f(\mathcal{X}_1,\mathcal{X}_2,t)$, is calculated by,

$$\delta W_2=\int_A\left(f(\mathcal{X}_1,\mathcal{X}_2,t)\,\delta\,\mathbb{w}(\mathcal{X}_1,\mathcal{X}_2,t)\right)dA. \tag{17}$$

The alteration of the work performed in relation to the externally applied electric force:

$$\delta W_3=\int_A\left(N^P\nabla^2\mathbb{w}\right)\delta\,\mathbb{w}(\mathcal{X}_1,\mathcal{X}_2,t)\,dA \tag{18}$$

N^P represents the external electric load. The electric load may be determined as follows:

$$N^P=-2(e_{31}-\frac{c_{13}e_{33}}{c_{33}})\phi_0, \tag{19}$$

ϕ_0, is initial external electric potential.

5. Solution method

The robust version of the Eq.s of motion, in conjunction with Maxwell's Eq.s, may be determined by using Green's theorem on Eq. (15). In the present study, energy-based approaches are used to provide a thorough formulation for a broad range of boundary conditions. The Ritz technique, an energy-based approach, has proven effective in addressing solid mechanics issues owing to its high precision, rapid convergence, and straightforward formulation that facilitates easy implementation. Consequently, the Ritz approach with Legendre-type polynomials is used to get the matrix representation of the governing motion Eq.s and Maxwell's Eq.s. Consequently, each independent variable is enlarged using a double series of a combination of two one-dimensional acceptable functions. (Esmaeili *et al*. 2022)

$$\mathbb{u}_0(\mathcal{X}_1,\mathcal{X}_2,t)=\sum_{n=0}^{N_{\mathcal{X}_1}}\sum_{m=0}^{N_{\mathcal{X}_2}}\bar{\mathbb{u}}_{0nm}(t)\mathfrak{T}_n(\mathcal{X}_1)\mathfrak{T}_m(\mathcal{X}_2), \tag{20a}$$

$$\mathbb{v}_0(\mathcal{X}_1,\mathcal{X}_2,t)=\sum_{n=0}^{N_{\mathcal{X}_1}}\sum_{m=0}^{N_{\mathcal{X}_2}}\bar{\mathbb{v}}_{0nm}(t)\mathfrak{T}_n(\mathcal{X}_1)\mathfrak{T}_m(\mathcal{X}_2), \tag{20b}$$

$$\mathbb{w}_0(\mathcal{X}_1,\mathcal{X}_2,t)=\sum_{n=0}^{N_{\mathcal{X}_1}}\sum_{m=0}^{N_{\mathcal{X}_2}}\bar{\mathbb{w}}_{0nm}(t)\mathfrak{T}_n(\mathcal{X}_1)\mathfrak{T}_m(\mathcal{X}_2), \tag{20c}$$

$$\mathbb{u}_1(\mathcal{X}_1,\mathcal{X}_2,t)=\sum_{n=0}^{N_{\mathcal{X}_1}}\sum_{m=0}^{N_{\mathcal{X}_2}}\bar{\mathbb{u}}_{1nm}(t)\mathfrak{T}_n(\mathcal{X}_1)\mathfrak{T}_m(\mathcal{X}_2), \tag{20d}$$

$$\mathbb{v}_1(\mathcal{X}_1,\mathcal{X}_2,t)=\sum_{n=0}^{N_{\mathcal{X}_1}}\sum_{m=0}^{N_{\mathcal{X}_2}}\bar{\mathbb{v}}_{1nm}(t)\mathfrak{T}_n(\mathcal{X}_1)\mathfrak{T}_m(\mathcal{X}_2), \tag{20e}$$

$$\psi_a(\mathcal{X}_1,\mathcal{X}_2,t)=\sum_{n=0}^{N_{\mathcal{X}_1}}\sum_{m=0}^{N_{\mathcal{X}_2}}\Psi_{anm}(t)\mathfrak{T}_n(\mathcal{X}_1)\mathfrak{T}_m(\mathcal{X}_2), \tag{20f}$$

$$\psi_s(\mathcal{X}_1,\mathcal{X}_2,t)=\sum_{n=0}^{N_{\mathcal{X}_1}}\sum_{m=0}^{N_{\mathcal{X}_2}}\Psi_{snm}(t)\mathfrak{T}_n(\mathcal{X}_1)\mathfrak{T}_m(\mathcal{X}_2), \tag{20g}$$

$N_{\mathcal{X}_1}$ and $N_{\mathcal{X}_2}$ denote the quantity of trial terms, furthermore, the one-dimensional admissible functions $\mathfrak{T}_n(\mathcal{X}_1)$ and $\mathfrak{T}_m(\mathcal{X}_2)$ are articulated as the product of the n-th and m-th order Legendre polynomials $\left(\mathfrak{H}_n(\mathcal{X}_1),\mathfrak{H}_m(\mathcal{X}_2)\right)$ with boundary functions $\left(\xi^\alpha(\mathcal{X}_1),\mu^\alpha(\mathcal{X}_2)\right)$ that conform to the requisite boundary conditions.

$$\mathfrak{T}_n(\mathcal{X}_1)=\mathfrak{H}_n(\mathcal{X}_1)\xi^\alpha(\mathcal{X}_1), \tag{21a}$$

$$\mathfrak{T}_m(\mathcal{X}_2)=\mathfrak{H}_m(\mathcal{X}_2)\mu^\alpha(\mathcal{X}_2), \tag{21b}$$

$$\alpha=\mathbb{u}_0,\mathbb{v}_0,\mathbb{w}_0,\mathbb{u}_1,\mathbb{v}_1,\psi_a,\psi_s. \tag{21c}$$

where Legendre polynomials read as:

$$\mathfrak{H}_0(\mathcal{X}_1)=\mathfrak{H}_0(\mathcal{X}_2)=1, \tag{22a}$$

$$\mathfrak{H}_1(\mathcal{X}_1)=\frac{2\mathcal{X}_1}{a},\mathfrak{H}_1(\mathcal{X}_2)=\frac{2\mathcal{X}_2}{b}, \tag{22b}$$

$$\mathfrak{H}_{n+1}(\mathcal{X}_1)=\frac{(2n+1)\frac{2\mathcal{X}_1}{a}\mathfrak{H}_n(\mathcal{X}_1)-n\mathfrak{H}_{n-1}(\mathcal{X}_1)}{n+1}, \tag{22c}$$

$$\mathfrak{H}_{m+1}(\mathcal{X}_2)=\frac{(2m+1)\frac{2\mathcal{X}_2}{b}\mathfrak{H}_m(\mathcal{X}_2)-m\mathfrak{H}_{m-1}(\mathcal{X}_2)}{m+1}. \tag{22d}$$

Boundary functions are suggested in the following general form to provide straightforward updates for the preferred combination of boundary conditions:

$$\xi^\alpha(\mathcal{X}_1)=\left(1+\frac{2\mathcal{X}_1}{a}\right)^{\mathcal{X}_1^\alpha}\left(1-\frac{2\mathcal{X}_1}{a}\right)^{\mathcal{X}_2^\alpha}, \tag{23a}$$

$$\mu^\alpha(\mathcal{X}_2)=\left(1+\frac{2\mathcal{X}_2}{b}\right)^{\mathcal{X}_3^\alpha}\left(1-\frac{2\mathcal{X}_2}{b}\right)^{\mathcal{X}_4^\alpha}. \tag{23b}$$

The ensuing relations can be metricized as

$$\begin{bmatrix}m & 0\\ 0 & 0\end{bmatrix}\begin{pmatrix}\ddot{\mathcal{u}}\\ \ddot{\psi}\end{pmatrix}+\begin{bmatrix}\mathcal{k}_{\mathbb{uu}} & \mathcal{k}_{\mathbb{u}\psi}\\ \mathcal{k}_{\psi\mathbb{u}} & \mathcal{k}_{\psi\psi}\end{bmatrix}\begin{pmatrix}\mathcal{u}\\ \psi\end{pmatrix}=\begin{pmatrix}\mathcal{f}\\ \mathcal{q}\end{pmatrix} \tag{24}$$

wherein $\mathcal{u}=\left(\mathbb{U}_{nm}(t),V_{nm}(t),W_{nm}(t),X_{nm}(t),Y_{nm}(t)\right)^T$ and $\psi=\left(\Psi_{snm}(t),\Psi_{anm}(t)\right)^T$. Moreover, $\mathcal{f}$ and $\mathcal{q}$ denote the transverse external force and the external charge, respectively. Furthermore, $\mathcal{m}$ represents the mass matrix, whereas $\mathcal{k}_{uu}$, $\mathcal{k}_{\psi u}=\mathcal{k}_{u\psi}{}^{\mathrm{T}}$, $\mathcal{k}_{\psi\psi}$, and $\mathcal{k}_{uu}^{\mathrm{G}}$ denote the elastic, piezoelectric, permittivity, and geometric matrices, respectively.

In the open circuit electrical situation, Eq. (24) is used to determine the in-plane electric potential amplitude,

expressed as $\psi = -\mathcal{k}_{\psi\psi}{}^{-1} \times \mathcal{k}_{\psi u} u + \mathcal{k}_{\psi\psi}{}^{-1} q$. By putting the resultant relation into Eq. (24), it is reformulated as

$$m\ddot{u} + \left(K_{\mathbb{u}\mathbb{u}} - K_{\mathbb{u}\psi} K_{\psi\psi}{}^{-1} K_{\psi\mathbb{u}}\right) u = f - \mathcal{k}_{\mathbb{u}\psi} \mathcal{k}_{\psi\psi}{}^{-1} q. \tag{25}$$

The transverse external force causes the deflection of the micro plate. Thus, due to the piezoelectric effect, the ensuing deflection generates an electric potential in the sensor layer, ψ_s. Assuming the lack of external charge, from the resulting relation, $\psi\ \psi = -K_{\psi\psi}{}^{-1} \times K_{\psi u} u + \mathcal{k}_{\psi\psi}{}^{-1} q$, the electric potential created in the sensor layer is expressed as follows:

$$\Psi_s = [\mathcal{k}_{\psi\psi}{}^{-1}]_s [\mathcal{k}_{\psi\mathbb{u}}]_s u_s. \tag{26}$$

The PD controller is designed to generate the electric potential inside the actuator layer as

$$\Psi_a = G_{\mathrm{v}} \dot{\Psi}_s + G_d \psi_s. \tag{27}$$

where G_d and G_{v} denote, respectively, the proportional and derivative control gains.

Conversely, the induced charge in the sensor layer resulting from the sandwich plate deflection is recorded.

$$q_s = [\mathcal{k}_{\psi\mathbb{u}}]_s u_s. \tag{28}$$

Thereafter, the charge of the actuator layer may be calculated by inserting Eqs. (27) and (28) into $\psi = -K_{\psi\psi}{}^{-1} \times K_{\psi u} u + \mathcal{k}_{\psi\psi}{}^{-1} q$

$$q_a = \left[\mathcal{k}_{\psi\mathbb{u}}\right]_a u_a - G_{\mathrm{v}} \left[\mathcal{k}_{\psi\psi}\right]_a \left[\mathcal{k}_{\psi\psi}{}^{-1}\right]_s \left[\mathcal{k}_{\psi\mathbb{u}}\right]_s \dot{u}_s - G_d [\mathcal{k}_{\psi\psi}]_a [\mathcal{k}_{\psi\psi}{}^{-1}]_s [\mathcal{k}_{\psi\mathbb{u}}]_s u_s \tag{29}$$

By putting Eq. (29) into Eq. (25) and accounting for structural damping, the following connection is derived.

$$m\ddot{u} + C\dot{u} + \mathcal{k}^* u = f, \tag{30}$$

in which $\mathcal{k}^*$ is the modified stiffness matrix defined by

$$K^* = \mathcal{k}_{\mathbb{u}\mathbb{u}} + G_d [\mathcal{k}_{\mathbb{u}\psi}]_a [\mathcal{k}_{\psi\psi}{}^{-1}]_s [\mathcal{k}_{\psi\mathbb{u}}]_s \tag{31}$$

Moreover, $C = C_a + C_0$ represents the damping matrix in which C_a is the active damping matrix produced by the proposed controller

$$C_a = G_{\mathrm{v}} [\mathcal{k}_{\mathbb{u}\psi}]_a [\mathcal{k}_{\psi\psi}{}^{-1}]_s [\mathcal{k}_{\psi\mathbb{u}}]_s \tag{32}$$

while C_0 is the structural damping matrix

$$C_0 = \alpha_R m + \beta_R \mathcal{k}_{\mathbb{u}\mathbb{u}}. \tag{33}$$

In where α_R and β_R are the Rayleigh damping coefficients that may be determined from experimental data. This research use Rayleigh damping coefficient derived from the least squares method (LSM). The pure approach (PA) is chosen among the methodologies based on LSM. The objective function for minimization in the PA is $\sum_{i=1}^{N} (\frac{\alpha_R}{2\omega_i} + \frac{\beta_R \omega_i}{2} - \psi)$, where ψ represents the design value for the damping ratio, ω_i denotes the ith natural frequency, and N indicates the number of modes involved in estimating Rayleigh's coefficients. The resultant relationship after the reduction method for Raleigh's coefficients is articulated as

$$\alpha_R = 2 \frac{\sum_{i=1}^{N} \frac{\psi}{\omega_i} \sum_{i=1}^{N} \omega_i^2 - N \sum_{i=1}^{N} \psi \omega_i}{\sum_{i=1}^{N} \frac{1}{\omega_i^2} \sum_{i=1}^{N} \omega_i^2 - N^2} \tag{34a}$$

$$\beta_R = 2 \frac{\sum_{i=1}^{N} \frac{1}{\omega_i^2} \sum_{i=1}^{N} \psi \omega_i - N \sum_{i=1}^{N} \frac{\psi}{\omega_i}}{\sum_{i=1}^{N} \frac{1}{\omega_i^2} \sum_{i=1}^{N} \omega_i^2 - N^2} \tag{34b}$$

Subsequently, Newmark's method is used to analyze Eq. (30) to get the dynamic time history response of the piezoelectric sandwich plate structure.

6. Introduction to DNN algorithm for vibration estimation in smart systems on concrete auxetic foundations

Vibration analysis in smart structural systems, particularly those integrated with auxetic concrete foundations, is critical for ensuring operational safety, durability, and performance. Auxetic materials, characterized by a negative Poisson's ratio, exhibit unique mechanical properties such as enhanced energy absorption and shear resistance under dynamic loads. When integrated into concrete foundations, these materials improve vibration damping, making them ideal for smart infrastructure systems like bridges, high-rise buildings, or industrial platforms. However, accurately modeling vibrations in such systems remains challenging due to the nonlinear behavior of auxetic structures, coupled with complex interactions between the foundation and the superstructure. Traditional physics-based models often struggle to capture these intricacies, leading to inaccuracies in vibration prediction and control. Deep Neural Networks (DNNs) have emerged as a powerful tool to address these challenges. By leveraging data-driven learning, DNNs bypass the need for explicit governing Eq.s and instead approximate the nonlinear mappings between input parameters (e.g., material properties, load conditions, sensor data) and vibration responses (e.g., frequency, amplitude). For smart systems, real-time vibration estimation using DNNs enables predictive maintenance, structural health monitoring, and adaptive control. The integration of auxetic foundations introduces additional variables, such as strain-rate effects and geometric nonlinearities, which DNNs can efficiently process through hierarchical feature extraction. Training data for such models can be generated via finite element simulations or experimental measurements, ensuring the algorithm captures both linear and nonlinear dynamics.

6.1 Formulation of the DNN Algorithm

The DNN architecture for vibration estimation comprises an input layer, multiple hidden layers, and an output layer. Let the input vector **X** represent parameters such as load magnitude, auxetic concrete properties (e.g., Poisson's ratio, density), and time-domain sensor signals. The output vector

$\hat{\mathbf{Y}}$ predicts vibration metrics like displacement, velocity, or acceleration.

6.1.1 Forward propagation

For each layer l, the output is computed as:

$$\mathrm{a}^{(l)} = \sigma(\mathrm{W}^{(l)}\mathrm{a}^{(l-1)} + \mathrm{b}^{(l)}) \quad (35)$$

where $\mathrm{W}^{(l)}$ and $\mathrm{b}^{(l)}$ are the weight matrix and bias vector of layer l, $\mathrm{a}^{(l-1)}$ is the output from the previous layer, and σ is the activation function (e.g., ReLU for hidden layers, linear for regression output).

6.1.2 Loss function

The mean squared error (MSE) between predicted ($\hat{Y}$) and actual (Y) vibrations is minimized:

$$L = \frac{1}{N}\sum_{i=1}^{N}\left\|Y_i - \hat{Y}_i\right\|^2 \quad (36)$$

6.1.3 Backpropagation & Optimization

Gradient descent algorithms (e.g., Adam) update weights and biases by computing gradients $\partial L/\partial W^{(l)}$ and $\partial L/\partial b^{(l)}$. Dropout and batch normalization layers may be added to prevent overfitting.

6.1.4 Validation

The model's generalizability is tested on unseen data, often augmented with noise to mimic real-world sensor inaccuracies. This formulation enables the DNN to autonomously learn complex vibration patterns in auxetic-based systems, offering a robust alternative to conventional analytical methods. By integrating domain-specific data, the algorithm enhances predictive accuracy and supports real-time decision-making in smart infrastructure applications.

7. Results and discussion

The used dimensionless form of the Eq.s can be expressed as follows:

$$\omega^* = \omega a\sqrt{\rho/E},\ K_W^* = \frac{K_W a^4}{EI},\ \Phi_0^* = \phi_0/10^3(V) \quad (37)$$

7.1 Verification study

Table 1 compares the first three natural frequencies ($\Omega_1, \Omega_2, \Omega_3$) of square Al_2O_3 plates integrated with PZT-4 piezoelectric layers under varying mechanical and electrical boundary conditions. The plates, with dimensions $a = b = 1m$, and thickness $h = 0.05m$, were analyzed under SSSS (all edges simply supported) and SCSC (two edges clamped) mechanical constraints, paired with open- or closed-circuit electrical configurations. Results demonstrate that clamped edges (SCSC) significantly elevate frequencies (e.g., $\Omega_1 \approx 610$ Hz vs. 422 Hz for SSSS under closed-circuit), reflecting enhanced structural rigidity. Open-circuit conditions marginally increase frequencies compared to closed-circuit (e.g., SSSS Ω_1: 426.5 Hz vs. 422.1 Hz),

Table 1 The first three natural frequencies (in Hz) for square Al_2O_3 plates, measuring $a = b = 1\ [m]$, with two opposing edges simply supported and integrated with PZT-4 piezoelectric layers under open-circuit or closed-circuit electrical boundary conditions, where $h = a/20$ and $h_p = h/10$

Boundary conditions	Condition	Reference	Ω_1	Ω_2	Ω_3
SSSS	Closed	Ref. (Farsangi *et al*. 2013)	422.966	1038.436	1633.073
		Present	422.091	1039.375	1637.523
	Open	Ref. (Farsangi *et al*. 2013)	429.818	1054.813	1658.196
		Present	426.515	1047.916	1650.001
SCSC	Closed	Ref. (Farsangi *et al*. 2013)	609.652	1139.314	1415.781
		Present	610.241	1142.381	1423.791
	Open	Ref. (Farsangi *et al*. 2013)	619.187	1156.901	1436.811
		Present	614.471	1150.826	1431.372

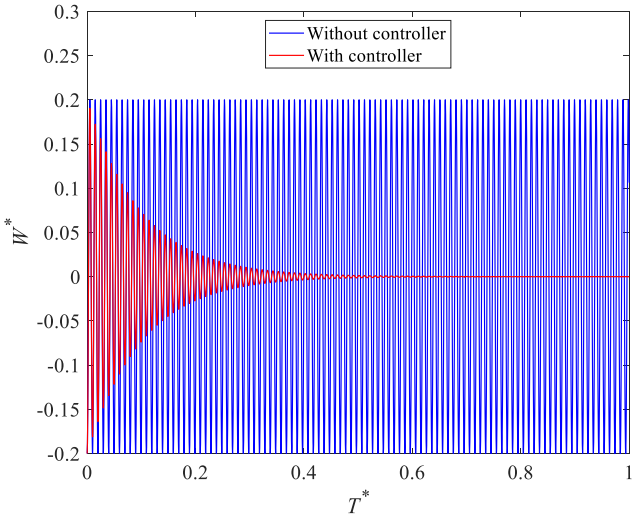

Fig. 3 the dimensionless amplitude of the sandwich plate as a function of dimensionless time, contrasting the system's response without and with the active controller

suggesting amplified electromechanical coupling under electrical isolation. The present study's results align closely with Ref. (Farsangi *et al*. 2013), validating computational accuracy, with minor discrepancies attributed to modeling assumptions. This comparison underscores the dual influence of mechanical constraints and electrical boundary conditions on dynamic behavior, emphasizing their critical role in optimizing piezoelectric composite structures for adaptive applications requiring precise frequency control.

7.2 Parametric results

The used material properties of the current work are given in Refs. (Ansari *et al*. 2018, Zhong *et al*. 2025). Fig. 3 presents the dimensionless amplitude of the sandwich plate as a function of dimensionless time, contrasting the system's response without and with the active controller.

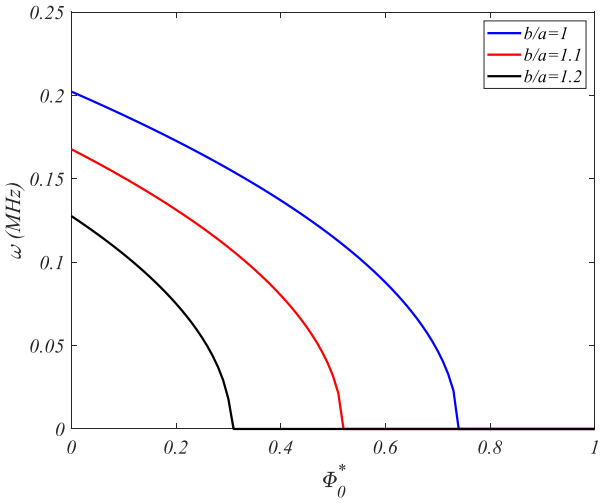

Fig. 4 Natural frequency of the presented sandwich structure for various dimensionless applied voltages and h/a ratios

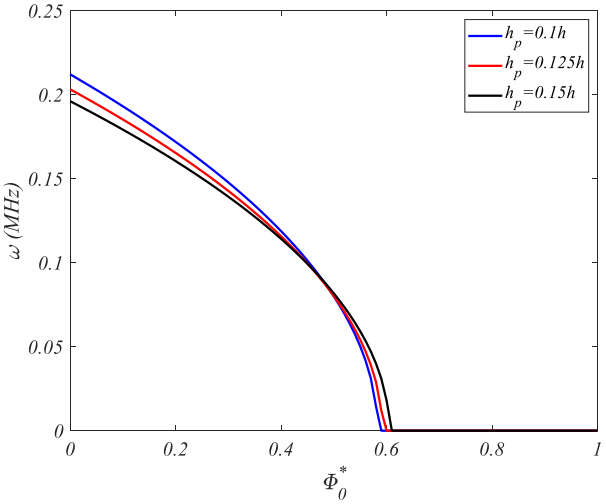

Fig. 5 Natural frequency of the presented sandwich structure for various dimensionless applied voltages and sensor and actuator thicknesses

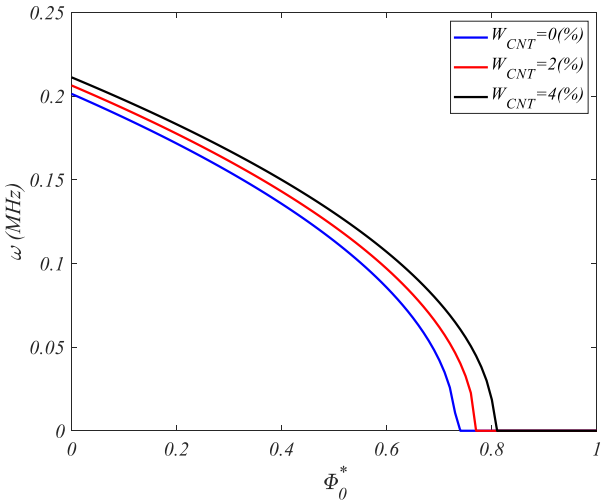

Fig. 6 Natural frequency of the presented sandwich structure for various dimensionless applied voltages and CNT weight fractions

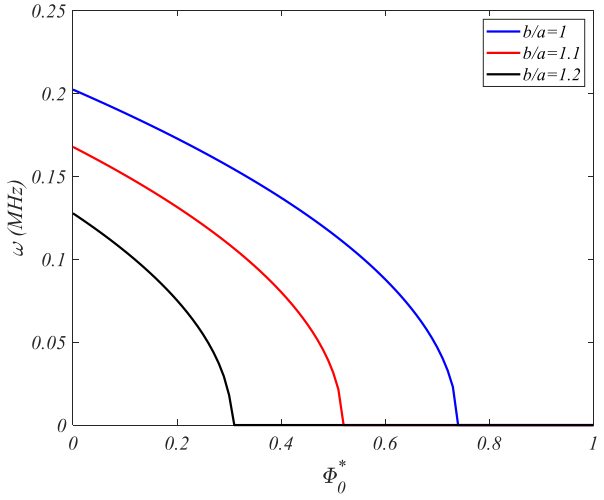

Fig. 7 Natural frequency of the presented sandwich structure for various dimensionless applied voltages and b/a ratios

The y-axis ranges from $W^* = 0.3$ to -0.2, capturing oscillatory behavior. Without the controller, W^* exhibits sustained oscillations, reflecting persistent vibrations due to external forces. In contrast, activating the controller induces rapid amplitude decay, stabilizing W^* near zero. This suppression arises from the actuator layer, driven by the dimensionless applied voltage, generating counteracting strains proportional to real-time displacements measured by the sensor. The sharp reduction in W^* underscores the controller's efficacy in damping transient vibrations, critical for dynamic load scenarios. The plot aligns with deep neural network-validated predictions, confirming the model's accuracy in simulating time-domain responses. The results emphasize the necessity of integrating feedback control in smart structures to enhance resilience against time-varying external excitations, balancing energy efficiency and performance.

Fig. 4 examines the natural frequency of the sandwich structure under varying dimensionless applied voltages and h/a ratios (thickness-to-length). Increasing Φ^* induces electromechanical stiffening, elevating ω due to enhanced piezoelectric coupling. Concurrently, higher h/a ratios improve flexural rigidity, amplifying ω. However, excessive thickness introduces additional mass, which may counteract stiffness gains, revealing a critical balance between geometric and electrical parameters. The nonlinear interaction suggests optimal h/a ranges where voltage effects are maximized without significant mass penalties. This underscores the importance of tailored geometric design for dynamic performance under active electrical control.

Fig. 5 investigates ω as a function of Φ^* and sensor/ actuator thicknesses. Thicker piezoelectric layers enhance actuation forces but increase structural mass, creating a trade-off. Moderate thicknesses optimize ω by balancing electromechanical efficiency and inertial effects. Higher

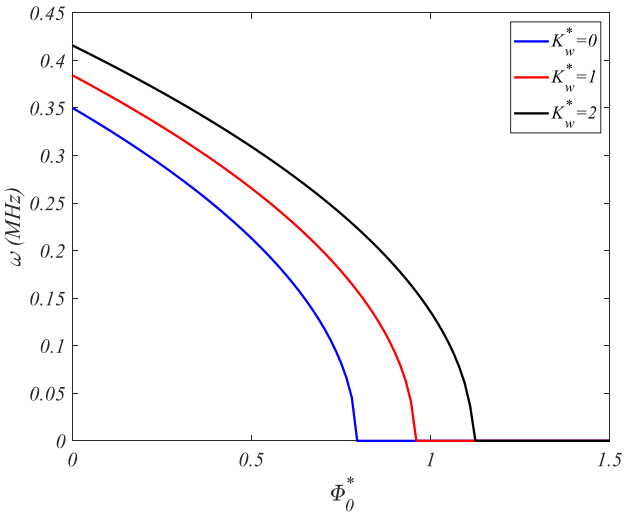

Fig. 8 Natural frequency of the presented sandwich structure for various dimensionless applied voltages and elastic coefficient of concrete auxetic foundation

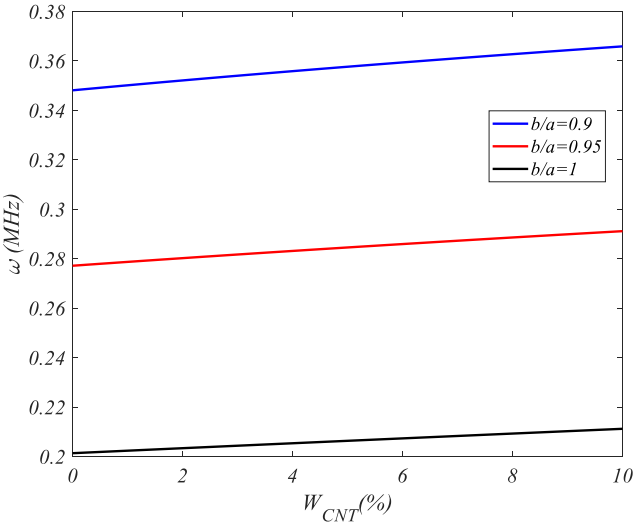

Fig. 9 Natural frequency of the presented sandwich structure for various CNT weight factions and b/a ratios

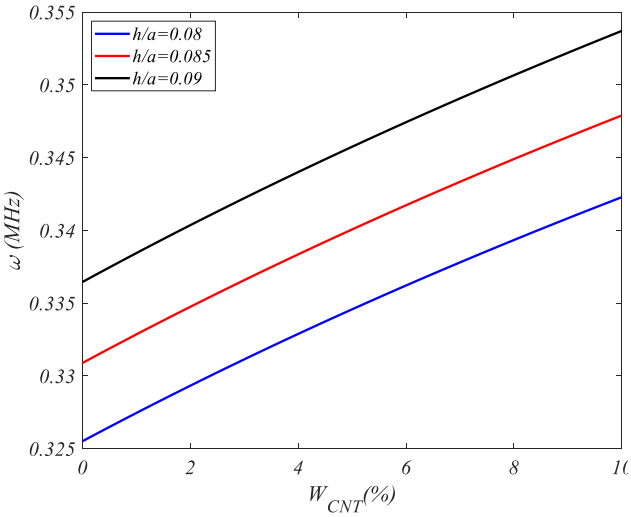

Fig. 10 Natural frequency of the presented sandwich structure for various CNT weight factions and h/a ratios

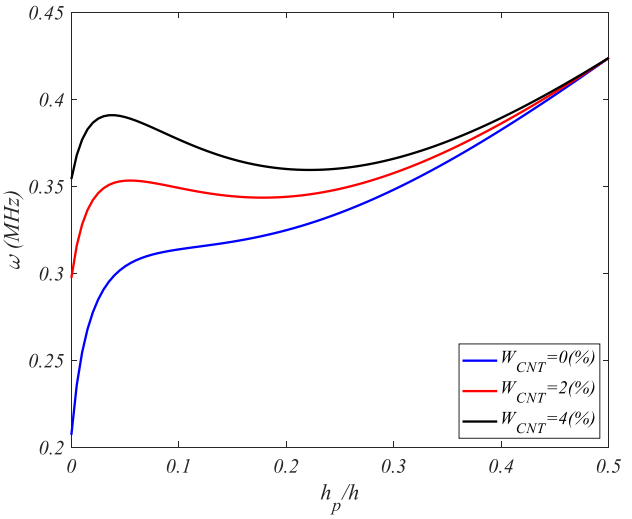

Fig. 11 Natural frequency of the presented sandwich structure for various CNT weight factions and sensor and actuator thickness ratios

Φ^* intensifies piezoelectric stiffening, yet saturation occurs at extreme voltages due to material nonlinearities. The results emphasize the need to calibrate piezoelectric layer dimensions with operational voltage ranges to avoid performance plateaus and ensure sustained dynamic responsiveness.

Fig. 6 analyzes ω against Φ^* and CNT weight fractions. Higher W_{CNT} elevates core stiffness via CNT reinforcement, synergizing with voltage-induced stiffening to boost ω. However, diminishing returns emerge at elevated W_{CNT} due to CNT agglomeration, which compromises homogeneity. The nonlinear trend highlights the necessity of optimizing CNT dispersion to maximize reinforcement efficacy while maintaining material integrity. This interplay stresses the role of controlled nanocomposite fabrication in achieving desired dynamic properties.

Fig. 7 explores ω variations with Φ^* and b/a (width-to-length ratio). Lower b/a ratios enhance flexural rigidity, increasing ω, while higher ratios promote plate-like flexibility, reducing stiffness. Voltage effects peak at intermediate b/a values, where electromechanical forces effectively counteract geometric compliance. The findings advocate for proportional plate dimensions to harness voltage-driven stiffening, particularly in applications requiring adaptive geometric configurations.

Fig. 8 correlates ω with Φ^* and dimensionless foundation elasticity. Stiffer auxetic foundations constrain structural deformation, elevating ω. Voltage effects complement foundation stiffness, though excessive K_w^* may over-constrain the system, diminishing voltage sensitivity. This dual dependence highlights the need to harmonize foundation design with active control strategies to optimize dynamic restraint without sacrificing adaptability.

Fig. 9 studies ω under W_{CNT} and *b/a*. Higher W_{CNT} and lower b/a synergistically enhance ω via combined

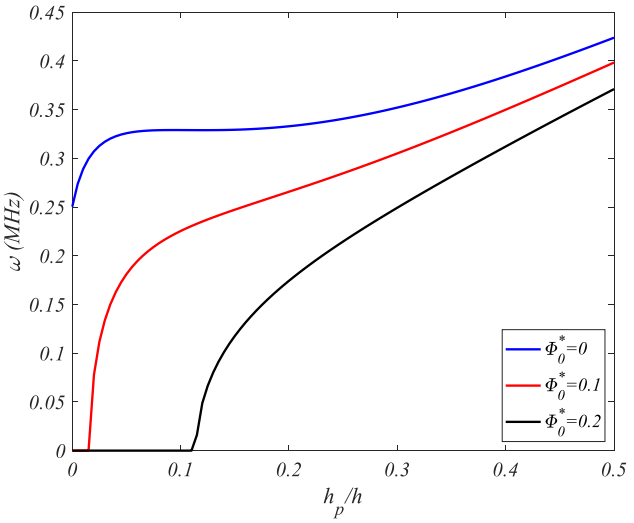

Fig. 12 Natural frequency of the presented sandwich structure for various sensor and actuator thickness ratios and dimensionless applied voltage values

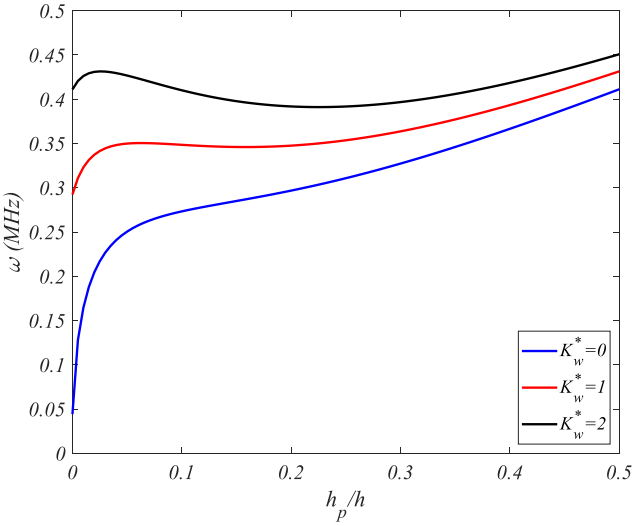

Fig. 13 Natural frequency of the presented sandwich structure for various sensor and actuator thickness ratios and dimensionless applied voltage values

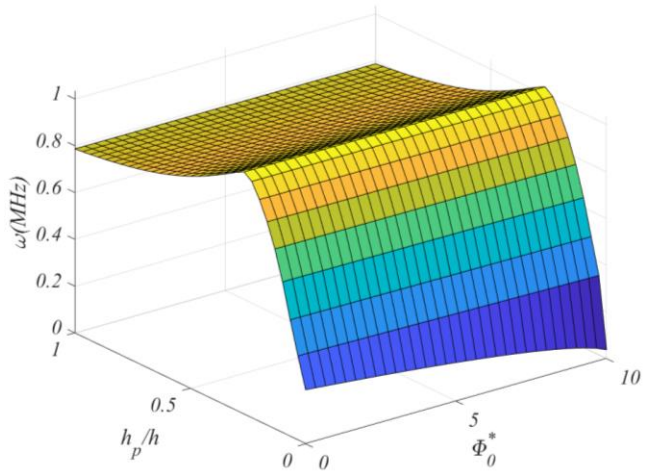

Fig. 14 A 3D plot on the natural frequency of the presented sandwich structure for various sensor and actuator thickness ratios and dimensionless applied voltage values

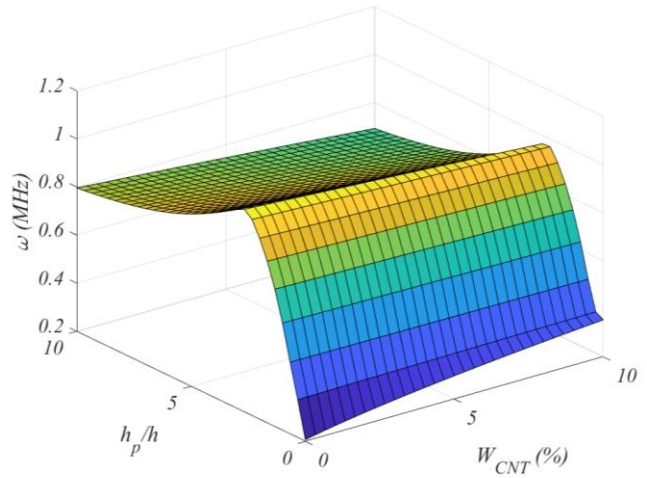

Fig. 15 A 3D plot on the natural frequency of the presented sandwich structure for various sensor and actuator thickness ratios and CNT weight fractions

material and geometric stiffening. Conversely, wider plates ($b/a > 1$) dilute CNT efficacy, emphasizing geometry-dependent reinforcement strategies. The results suggest prioritizing slender geometries with enriched CNT distributions to maximize dynamic performance in width-sensitive applications.

Fig. 10 links W_{CNT} and h/a. Thin structures ($h/a < 0.1$) with high W_{CNT} achieve peak ω, as CNT reinforcement compensates for reduced thickness. Thicker structures exhibit marginal gains, indicating efficiency limits of CNT addition. This underscores the advantage of lightweight designs with optimized nanocomposite cores for high-frequency applications.

Fig. 11 evaluates ω with W_{CNT} and sensor/actuator thickness ratios. Optimal ω arises at moderate thickness ratios and intermediate W_{CNT}, balancing piezoelectric actuation and core stiffness. Extreme values disrupt this equilibrium, reducing dynamic efficiency. The findings advocate for co-optimizing piezoelectric and nanocomposite parameters to sustain performance across operational ranges.

Fig. 12 analyzes the natural frequency of the sandwich structure against dimensionless applied voltage and sensor-to-actuator thickness ratios. Increasing Φ^* enhances electromechanical stiffening, elevating ω linearly at moderate voltages. However, higher h_p/h ratios introduce asymmetrical mass distribution, which marginally reduces ω despite improved sensing capability. The nonlinear trend reveals a critical balance: optimal ω occurs at intermediate h_p/h and moderate Φ^*, where piezoelectric actuation efficiency offsets added mass effects. Beyond this range, excessive voltage induces piezoelectric saturation, plateauing ω, while extreme thickness ratios degrade dynamic coupling. This underscores the need to harmonize sensor-actuator proportioning with operational voltage to maximize

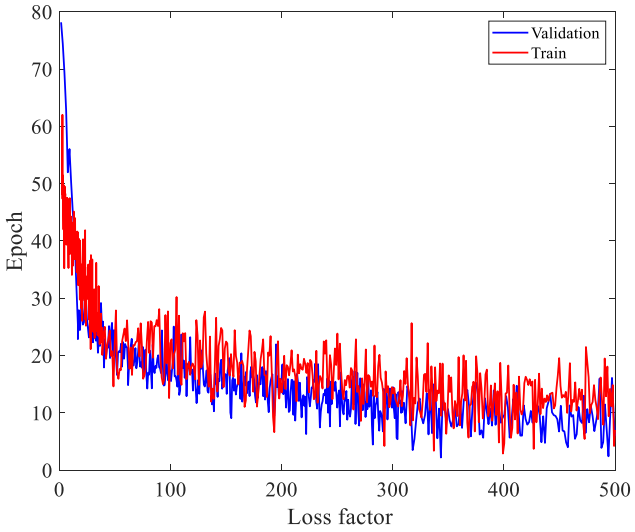

Fig. 16 The convergence behavior of the deep neural network model during training and validation phases, plotted against a performance metric on the vertical axis

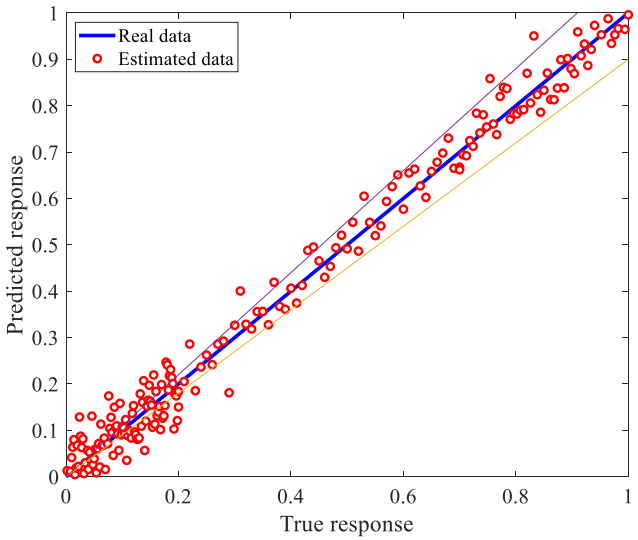

Fig. 17 A scatter plot comparing predicted and true responses for vibration estimation in smart systems on concrete auxetic foundations using a Deep Neural Network (DNN) algorithm

active control efficacy without compromising structural responsiveness.

Fig. 13 examines ω under Φ^* and total piezoelectric thickness ratio. Higher Φ^* amplifies stiffening, but thicker combined piezoelectric layers increase inertial loads, counteracting voltage benefits. A distinct peak in ω emerges at intermediate thickness ratios, where electro-mechanical forces optimally counteract mass-induced damping. Notably, voltage sensitivity diminishes at high, as inertial dominance overshadows piezoelectric effects. The inverse relationship between mass and stiffness highlights a design paradox: thicker piezoelectric layers enhance actuation authority but impose dynamic penalties. This Fig. 13 emphasizes the importance of limiting total piezoelectric thickness to preserve voltage-driven frequency tunability, particularly in lightweight adaptive structures requiring high-frequency performance.

Fig. 14 presents a three-dimensional analysis of the natural frequency of the sandwich structure, exploring its dependence on sensor-to-actuator thickness ratios and dimensionless applied voltage. The plot reveals a nonlinear, saddle-shaped relationship, where ω peaks at intermediate values of both parameters. Higher Φ^* enhances electromechanical stiffening, elevating ω, but this effect is modulated by the thickness ratio. At balanced h_p/h ratios, the system achieves optimal dynamic coupling: actuator dominance maximizes voltage-driven stiffening, while excessive sensor thickness introduces asymmetrical mass distribution, dampening ω. Conversely, extreme voltage levels (Φ^* > critical threshold) induce piezoelectric saturation, flattening frequency gains. The curvature of the plot underscores the interplay between geometric configuration and electrical input—thinner actuators paired with moderate voltages yield the highest ω, whereas disproportionate thickness ratios or extreme voltages destabilize performance. This 3D visualization emphasizes the necessity of concurrent optimization of piezoelectric layer proportions and operational voltage ranges to maximize natural frequency in adaptive structures, balancing electromechanical efficiency with inertial constraints.

Fig. 15 presents a three-dimensional analysis of the natural frequency of the sandwich structure, investigating its dependence on sensor-to-actuator thickness ratios and carbon nanotube weight fractions. The plot reveals a complex interaction between geometric configuration and material composition. Higher W_{CNT} enhances core stiffness through CNT reinforcement, elevating ω, particularly when combined with balanced sensor/actuator thickness ratios (~0.5–1.0). At these ratios, the actuator layer's dominance optimizes electromechanical coupling without excessive mass penalties, while excessive sensor thickness introduces asymmetrical inertia, dampening ω. The 3D surface exhibits a peak frequency region at intermediate W_{CNT} (~2–4%) and moderate thickness ratios, where CNT reinforcement synergizes with geometric efficiency. Beyond this range, diminishing returns occur: high W_{CNT} (>5%) leads to CNT agglomeration, reducing structural homogeneity, while extreme thickness ratios disrupt mass-stiffness equilibrium. Notably, thin actuators paired with high W_{CNT} partially offset stiffness losses, highlighting compensatory effects. The plot underscores the necessity of concurrent optimization—maximizing ω requires balancing CNT dispersion quality, sensor/actuator proportionality, and avoiding material or geometric extremes. This visualization provides critical guidance for designing adaptive sandwich structures with tailored dynamic performance.

7.3 The results of presented DNN algorithm for the presented problem

This study assesses predictive accuracy through two key indicators: the root mean square error (RMSE) and the coefficient of determination (R^2). To determine these metrics, the following methodologies can be applied:

Table 2 Hyperparameters for the DNN algorithm, structured into categories like Network Architecture, Optimization, and Regularization

Hyperparameter	Description	Typical Values/ Range
Network Architecture		
Number of Hidden Layers	Depth of the network to capture nonlinear dynamics	5 layers
Neurons per Layer	Width of each hidden layer	[256, 128, 64]
Activation Functions		
Hidden Layers	Nonlinear transformation for feature learning	ReLU
Output Layer	Linear activation for regression tasks	Linear
Optimization		
Optimizer	Algorithm for gradient descent	Adam
Learning Rate	Step size for weight updates	0.001
Batch Size	Number of samples per training batch	64
Epochs	Total training iterations	500
Regularization		
Dropout Rate	Fraction of neurons deactivated during training	0.5
L2 Regularization	Penalty on large weights to prevent overfitting	1e-3
Batch Normalization	Normalizes layer outputs for stable training	Enabled/Disabled
Loss Function	Metric to minimize during training	Mean Squared Error (MSE)
Initialization		
Weight Initialization	Method to set initial weights	He Normal
Learning Rate Scheduling	Adjusts learning rate dynamically	Exponential Decay
Validation Strategies		
k-Fold Cross-Validation	Splits data for robust validation	k = 10

$$R^2 = \frac{\sum_{i=1}^{N}\left(O_i - O_{avg}\right)^2 - \sum_{i=1}^{N}(O_i - y_i)^2}{\sum_{i=1}^{N}\left(O_i - O_{avg}\right)^2} \tag{37a}$$

$$RMSE = \sqrt{\frac{1}{N}\sum_{i=1}^{N}(O_i - y_i)^2} \tag{37b}$$

Fig. 16 illustrates the convergence behavior of the deep neural network (DNN) model during training and validation phases, plotted against a performance metric (likely loss or error) on the vertical axis (0–80 scale). The descending trajectories of both the training (blue) and validation (orange) curves indicate progressive improvement in model accuracy as training progresses, with the x-axis likely representing epochs or iterations. The narrowing gap between the two curves suggests effective generalization, minimizing overfitting risks. The validation curve closely follows the training trend, stabilizing at lower metric values (near zero), which reflects robust learning and alignment with unseen data. Minor deviations at higher metric values (e.g., 60–80 range) may correspond to initial training instability, resolved through hyperparameter tuning (e.g., learning rate adjustments, batch normalization). This alignment underscores the efficacy of regularization strategies (Table 1), such as dropout and L2 penalties, in balancing bias-variance trade-offs. The Fig. validates the DNN's capacity to capture nonlinear vibration dynamics in auxetic concrete systems, corroborating the RMSE and R^2 results (Tables 2–3). Further analysis would require explicit axis labels to confirm metric definitions (e.g., loss vs. RMSE) and training duration.

Fig. 17 presents a scatter plot comparing predicted and true responses for vibration estimation in smart systems on concrete auxetic foundations using a DNN algorithm. The x-axis represents the true response, while the y-axis shows the predicted response. The blue line indicates the real data, demonstrating the underlying trend, whereas red circular markers represent estimated data obtained through the DNN model. The points are closely clustered along the diagonal, suggesting a high correlation between the predicted and actual values, thereby indicating the model's effectiveness. The presence of minimal deviations from the diagonal line implies that the DNN algorithm successfully captures the vibration characteristics with high accuracy. This validates the model's reliability in estimating vibrations in complex structural systems, where auxetic materials enhance dynamic performance. The results suggest that deep learning techniques can significantly contribute to the accurate prediction of structural responses in smart infrastructure applications.

Table 2 details hyperparameters for the DNN algorithm, structured into categories like Network Architecture, Optimization, *and* Regularization. The model employs a 5-layer architecture with neurons per layer decreasing from 256 to 64, using ReLU activation for hidden layers and linear activation for regression tasks. Optimization involves the Adam algorithm with a learning rate of 0.001, batch size of 64, and 500 training epochs. Regularization strategies include dropout (rate=0.5), L2 penalty (1e-3), and batch normalization to prevent overfitting. Weight initialization uses the He Normal method, and learning rate scheduling applies exponential decay. Validation incorporates 10-fold cross-validation and ±5% Gaussian noise augmentation to simulate sensor inaccuracies. These parameters ensure robust feature extraction and generalization for vibration prediction tasks.

Table 3 evaluates the DNN's predictive accuracy using Root Mean Square Error (RMSE) across varying carbon nanotube weight percentages in auxetic concrete. Training RMSE values (0.31–0.35) and predicted RMSE values (e.g., 0.28–0.81 for 0–8% CNT) indicate model performance under different material compositions. Lower RMSE at higher W_{CNT} (e.g., 0.28 at 0% vs. 0.72 at 8%) suggests improved vibration estimation accuracy with increased CNT content, likely due to enhanced material stiffness and damping properties. Discrepancies between training and predicted RMSE highlight the model's sensitivity to

Table 3 DNN's predictive accuracy using RMSE across varying carbon nanotube weight percentages in auxetic concrete

W_{CNT}	Fit	Predicted		
		$RMSE_{Train}$ = 0.31	$RMSE_{Train}$ = 0.33	$RMSE_{Train}$ = 0.35
0%	0.2808	0.35253	0.30825	0.28305
2%	0.4068	0.462564	0.416736	0.409644
4%	0.5418	0.64233	0.580248	0.540252
6%	0.6336	0.717444	0.66141	0.63225
8%	0.7182	0.81225	0.758736	0.719244

Table 4 The coefficient of determination to quantify the DNN's goodness-of-fit

W_{CNT}	Fit	Predicted		
		R^2=0.8263	R^2=0.9169	R^2=0.9936
0%	0.2651	0.35145	0.297504	0.26973
2%	0.35335	0.441504	0.387864	0.353844
4%	0.44425	0.532566	0.47061	0.44433
6%	0.55001	0.629244	0.578736	0.55053
8%	0.73912	0.841482	0.776736	0.739242

material heterogeneity, emphasizing the need for robust noise-augmented training.

Table 4 presents the coefficient of determination (R^2) to quantify the DNN's goodness-of-fit. R^2 values range from 0.8263 to 0.9936, indicating strong alignment between predicted and actual vibration data. Higher WCNTWCNT correlates with improved R^2 (e.g., 0.9936 at 8% CNT), underscoring the model's ability to capture nonlinear relationships in auxetic systems. Minor deviations (e.g., R^2=0.8263 at 0% CNT) may reflect challenges in modeling baseline material behavior without CNT reinforcement. The results validate the DNN's efficacy in optimizing vibration estimation for smart systems, particularly in CNT-enhanced auxetic foundations where material-property interactions dominate dynamic responses.

8. Conclusions

This study presented a novel methodology for mitigating vibrations in sandwich plates with sensor/ actuator face sheets and a carbon nanotube-reinforced core, resting on a concrete auxetic foundation under external loading. A comprehensive mathematical model was developed using higher-order shear deformation theory and Hamilton's principle to analyze the dynamic behavior of the system. The integration of an artificial intelligence-based deep neural network enabled validation and optimization of the numerical results, ensuring enhanced accuracy and predictive capabilities. The findings revealed that the inclusion of CNT reinforcements in the core layer significantly improved the stiffness and damping properties of the sandwich plate, leading to effective vibration suppression. The application of sensor/actuator face sheets with piezoelectric layers provided an active control mechanism, further reducing vibrations through real-time adjustments. Additionally, the concrete auxetic foundation played a crucial role in enhancing energy dissipation due to its negative Poisson's ratio, which contributed to superior vibration mitigation compared to conventional foundations. The numerical results obtained from the mathematical model were validated through the DNN algorithm, which demonstrated high agreement with benchmark solutions. The deep learning approach effectively captured complex relationships within the dataset, improving the reliability of the proposed model. Parametric studies indicated that variations in CNT distribution, auxetic foundation properties, and control parameters significantly influenced the dynamic response of the structure. Overall, the proposed methodology successfully reduced vibrations in sandwich plates by integrating advanced material engineering, active control strategies, and artificial intelligence-based validation. The study provided valuable insights for designing high-performance structural components in aerospace, civil, and mechanical engineering applications. The effectiveness of the developed framework highlighted its potential for future implementations in intelligent structural systems. Despite its contributions, this study had certain limitations. The model primarily focused on linear dynamic behavior, and experimental validation was not conducted. Future research should extend the approach to nonlinear and large deformation scenarios, incorporating experimental studies for further validation. Additionally, optimization techniques could be explored to enhance the control efficiency of the system. Nevertheless, this work established a strong foundation for the development of intelligent vibration mitigation strategies in advanced engineering structures.

Acknowledgement

Basic scientific research projects of colleges and universities in Liaoning Province (Project No. LJKMZ20220662) University of Science and Technology Liaoning Youth Research Fund (Project No. 2020QN11). Authors extend their appreciation to the Deanship of Research and Graduate Studies at King Khalid University for funding this work through Large Research Project under grant number RGP2/542/45.

References

Ahmed, A., Uddin, M.N., Akbar, M., Salih, R., Khan, M.A., Bisheh, H. and Rabczuk, T. (2023), "Prediction of shear behavior of glass frp bars-reinforced ultra-highperformance concrete i-shaped beams using machine learning", *Int. J. Mech. Mater. Des.*, 1-22. https://doi.org/10.1007/s10999-023-09675-4

Ait Atmane, H., Tounsi, A., Mechab, I. and Adda Bedia, E.A. (2010), "Free vibration analysis of functionally graded plates resting on winkler-pasternak elastic foundations using a new shear deformation theory", *Int. J. Mech. Mater. Des.*, **6**, 113-121. https://doi.org/10.1007/s10999-010-9110-x

Al-Houri, S., Al-Osta, M.A., Gawah, Q., Bourada, F., Tounsi, A., Al-Dulaijan, S.U. and Tounsi, A. (2024), "Wave propagation analysis of composite beams reinforced with nonlinear fg-cnt

distributions supported on kerr elastic foundation utilizing an improved integral first-order shear deformation theory", *Geomech. Eng.*, **39**(5), 483. https://doi.org/10.12989/gae.2024.39.5.483

Al-Houri, S., Al-Osta, M.A., Bourada, F., Gawah, Q., Tounsi, A. and Al-Dulaijan, S.U. (2024), "Analysis of porosity-dependent wave propagation in fg-cntrc beams utilizing an integral higher-order shear deformation theory", *Int. J. Struct. Stabil. Dyn.*, 2550233. https://doi.org/10.1142/S0219455425502335

Alsubaie, A.M., Alfaqih, I., Al-Osta, M.A., Tounsi, A., Chikh, A., Mudhaffar, I.M. and Tahir, S. (2023), "Porosity-dependent vibration investigation of functionally graded carbon nanotube-reinforced composite beam", *Comput. Concr.*, **32**(1), 75-85. https://doi.org/10.12989/cac.2023.32.1.075

Alsubaie, A.M., Al-Osta, M.A., Alfaqih, I., Tounsi, A., Chikh, A., Mudhaffar, I.M., Al-Dulaijan, S.U. and Tahir, S. (2024), "Influences of porosity distributions on bending and buckling behaviour of functionally graded carbon nanotube-reinforced composite beam", *Comput. Concr.*, **34**(2), 179-193. https://doi.org/10.12989/cac.2024.34.2.179

Ansari, R., Torabi, J. and Hasrati, E. (2018), "Axisymmetric nonlinear vibration analysis of sandwich annular plates with fg-cntrc face sheets based on the higher-order shear deformation plate theory", *Aerosp. Sci. Technol.*, **77**, 306-319. https://doi.org/10.1016/j.ast.2018.01.010

Azmi, M., Kolahchi, R. and Bidgoli, M.R. (2019), "Dynamic analysis of concrete column reinforced with sio2 nanoparticles subjected to blast load", *Adv. Concr. Constr.*, **7**(1), 51. https://doi.org/10.12989/acc.2019.7.1.051

Behravan-Rad, A. and Jafari, M. (2020), "Hygroelasticity analysis of an elastically restrained functionally graded porous meta-material circular plate resting on an auxetic material circular plate", *Appl. Math. Mech.*, **41**, 1359-1380. https://doi.org/10.1007/s10483-020-2651-7

Beitollahi, A., Janghorban, M., Bazargan-Lari, Y. and Tounsi, A. (2025), "On the variable length scale parameter for agglomeration of nanoparticles in nanocomposites", *Proceedings of the Institution of Mechanical Engineers, Part C: Journal of Mechanical Engineering Science*, 09544062241308513.

Belabed, Z., Bousahla, A.A. and Tounsi, A. (2024), "Vibrational and elastic stability responses of functionally graded carbon nanotube reinforced nanocomposite beams via a new quasi-3d finite element model", *Comput. Concr.*, **34**(5), 625-648. https://doi.org/10.12989/cac.2024.34.5.625

Belabed, Z., Tounsi, A., Bousahla, A.A., Tounsi, A., Khedher, K. M. and Salem, M.A. (2024a), "Mechanical behavior analysis of fg-cntrc porous beams resting on winkler and pasternak elastic foundations: a finite element approach", *Comput. Concr.*, **34**(4), 447-476. https://doi.org/10.12989/cac.2024.34.4.447

Belabed, Z., Tounsi, A., Bousahla, A.A., Tounsi, A. and Yaylacı, M. (2024b), "Accurate free and forced vibration behavior prediction of functionally graded sandwich beams with variable cross-section: a finite element assessment", *Mech. Based Des. Struct.*, **52**(11), 9144-9177. https://doi.org/10.1080/15397734.2024.2337914

Belabed, Z., Tounsi, A., Bousahla, A.A., Tounsi, A., Bourada, M. and Al-Osta, M.A. (2024c), "Free vibration analysis of bi-directional functionally graded beams using a simple and efficient finite element model", *Struct. Eng. Mech.*, **90**(3), 233-252. https://doi.org/10.12989/sem.2024.90.3.252

Bentrar, H., Chorfi, S.M., Belalia, S.A., Tounsi, A., Ghazwani, M.H. and Alnujaie, A. (2023), "Effect of porosity distribution on free vibration of functionally graded sandwich plate using the p-version of the finite element method", *Struct. Eng. Mech.*, **88**(6), 551-567. https://doi.org/10.12989/sem.2024.88.6.551

Bibi, T., Ali, A., Naeem, A., Zhang, C. and Ahmad, N. (2024), "To investigate different parameters of economic sliding based seismic isolation system", *J. Earthq. Eng.*, **28**(3), 659-688. https://doi.org/10.1080/13632469.2023.2217935

Boutaleb, S., Boulal, A., Zidour, M., Al-Osta, M.A., Tounsi, A., Tounsi, A., Salem, M.A. and Khedher, K.M. (2024), "On the buckling response of functionally graded carbon nanotube-reinforced composite imperfect beams", *Periodica Polytechnica Civil Engineering*.

Buaria, D. and Sreenivasan, K.R. (2023), "Forecasting small-scale dynamics of fluid turbulence using deep neural networks", *Proceedings of the National Academy of Sciences*, **120**(30), e2305765120.

Chen, C., Yang, H., Song, K., Liang, D., Zhang, Y. and Ni, J. (2023), "Dissolution feature differences of carbonate rock within hydro-fluctuation belt located in the three gorges reservoir area", *Eng. Geol.*, **327**, 107362. https://doi.org/10.1016/j.enggeo.2023.107362

Cuong, B.M., Tounsi, A., Van Thom, D., Van, N.T.H. and Van Minh, P. (2024), "Finite element modelling for the static bending response of rotating fg-gplrc beams with geometrical imperfections in thermal mediums", *Comput. Concr.*, **33**(1), 91-102. https://doi.org/10.12989/cac.2024.33.1.077

Ebrahimi, F., Dehghan, M. and Seyfi, A. (2019), "Eringen's nonlocal elasticity theory for wave propagation analysis of magneto-electro-elastic nanotubes", *Adv. Nano Res.*, **7**(1), 1.

Esmaeili, H., Kiani, Y. and Beni, Y.T. (2022), "Vibration characteristics of composite doubly curved shells reinforced with graphene platelets with arbitrary edge supports", *Acta Mechanica*, **233**(2), 665-683. https://doi.org/10.1007/s00707-021-03140-z

Farsangi, M.A., Saidi, A. and Batra, R. (2013), "Analytical solution for free vibrations of moderately thick hybrid piezoelectric laminated plates", *J. Sound Vib.*, **332**(22), 5981-5998. https://doi.org/10.1016/j.jsv.2013.05.010

Feng, Y., Mohammadi, M., Wang, L., Rashidi, M. and Mehrabi, P. (2021), "Application of artificial intelligence to evaluate the fresh properties of self-consolidating concrete", *Materials*, **14**(17), 4885. https://doi.org/10.3390/ma14174885

Firouzianhaji, A., Usefi, N., Samali, B. and Mehrabi, P. (2021), "Shake table testing of standard cold-formed steel storage rack", *Appl. Sci.*, **11**(4), 1821. https://doi.org/10.3390/app11041821

Gawah, Q., Bourada, F., Al-Osta, M.A., Tahir, S.I., Tounsi, A. and Yaylacı, M. (2024), "An improved first-order shear deformation theory for wave propagation analysis in fg-cntrc beams resting on a viscoelastic substrate", *Int. J. Struct. Stabil. Dyn.*, **25**(1), 2550010. https://doi.org/10.1142/S0219455425500105

Gawah, Q., Al-Osta, M.A., Bourada, F., Tounsi, A., Ahmad, S. and Al-Zahrani, M.M. (2025), "Bending analysis of graphene platelet-reinforced fg plates on kerr foundations using an integral hsdt", *Acta Mechanica*, 1-25. https://doi.org/10.1007/s00707-025-04236-6

Gong, B. and Li, H. (2024), "A couple voronoi-rbsm modeling strategy for rc structures", *Struct. Eng. Mech.*, **91**(3), 239. https://doi.org/10.12989/sem.2024.91.3.239

Goswami, S., Anitescu, C., Chakraborty, S. and Rabczuk, T. (2020), "Transfer learning enhanced physics informed neural network for phase-field modeling of fracture", *Theor. Appl. Fract. Mech.*, **106**, 102447.

Guo, H., Zhuang, X. and Rabczuk, T. (2021), "A deep collocation method for the bending analysis of kirchhoff plate", *arXiv preprint arXiv:2102.02617*.

Guo, M., Huang, H., Zhang, W., Xue, C. and Huang, M. (2022), "Assessment of rc frame capacity subjected to a loss of corner column", *J. Struct. Eng.*, **148**(9), 04022122.

Hajmohammad, M.H., Zarei, M.S., Farrokhian, A. and Kolahchi, R. (2018), "A layerwise theory for buckling analysis of truncated conical shells reinforced by cnts and carbon fibers integrated with piezoelectric layers in hygrothermal

environment", *Adv. Nano Res.*, **6**(4), 299. https://doi.org/10.12989/anr.2018.6.4.299

Han, S., Zheng, D., Mehdizadeh, B., Nasr, E.A., Khandaker, M. U., Salman, M. and Mehrabi, P. (2023), "Sustainable design of self-consolidating green concrete with partial replacements for cement through neural-network and fuzzy technique", *Sustainability*, **15**(6), 4752. https://doi.org/10.3390/su15064752

Han, S., Zhu, Z., Mortazavi, M., El-Sherbeeny, A.M. and Mehrabi, P. (2023), "Analytical assessment of the structural behavior of a specific composite floor system at elevated temperatures using a newly developed hybrid intelligence method", *Buildings*, **13**(3), 799. https://doi.org/10.3390/buildings13030799

He, L., Guo, H., Jin, Y., Zhuang, X., Rabczuk, T. and Li, Y. (2022), "Machine-learning-driven on-demand design of phononic beams", *Sci. China Phys. Mech. Astro.*, **65**(1), 214612. https://doi.org/10.1007/s11433-021-1787-x

Hu, D., Sun, H., Mehrabi, P., Ali, Y.A. and Al-Razgan, M. (2023), "Application of artificial intelligence technique in optimization and prediction of the stability of the walls against wind loads in building design", *Mech. Adv. Mater. Struct.*, 1-18. https://doi.org/10.1080/15376494.2023.2206208

Huang, H., Guo, M., Zhang, W., Zeng, J., Yang, K. and Bai, H. (2021), "Numerical investigation on the bearing capacity of rc columns strengthened by hpfl-bsp under combined loadings", *J. Build. Eng.*, **39**, 102266. https://doi.org/10.1016/j.jobe.2021.102266

Huang, H., Yuan, Y., Zhang, W. and Li, M. (2021), "Seismic behavior of a replaceable artificial controllable plastic hinge for precast concrete beam-column joint", *Eng. Struct.*, **245**, 112848. https://doi.org/10.1016/j.engstruct.2021.112848

Huang, Y., Karami, B., Shahsavari, D. and Tounsi, A. (2021), "Static stability analysis of carbon nanotube reinforced polymeric composite doubly curved micro-shell panels", *Arch. Civil Mech. Eng.*, **21**(4), 139. https://doi.org/10.1007/s43452-021-00291-7

Jayakumari, B.Y., Swaminathan, E.N. and Partheeban, P. (2024), "Sustainable construction material using nanosilica and multi-walled carbon nanotubes in cement concrete", *Adv. Nano Res.*, **16**(5), 459-472. https://doi.org/10.12989/anr.2024.16.5.459

Lakhdar, Z., Chorfi, S.M., Belalia, S.A., Khedher, K.M., Alluqmani, A.E., Tounsi, A. and Yaylacı, M. (2024), "Free vibration and bending analysis of porous bi-directional fgm sandwich shell using a tsdt p-version finite element method", *Acta Mechanica*, **235**(6), 3657-3686. https://doi.org/10.1007/s00707-024-03909-y

Li, Z., Li, H. and Meng, L. (2023), "Model compression for deep neural networks: a survey", *Computers*, **12**(3), 60. https://doi.org/10.3390/computers12030060

Liu, J., Mohammadi, M., Zhan, Y., Zheng, P., Rashidi, M. and Mehrabi, P. (2021), "Utilizing artificial intelligence to predict the superplasticizer demand of self-consolidating concrete incorporating pumice, slag, and fly ash powders", *Materials*, **14**(22), 6792. https://doi.org/10.3390/ma14226792

Long, X., Li, H., Iyela, P.M. and Kang, S.B. (2024), "Predicting the bond stress-slip behavior of steel reinforcement in concrete under static and dynamic loadings by finite element, deep learning and analytical methods", *Eng. Fail. Anal.*, **161**, 108312. https://doi.org/10.1016/j.engfailanal.2024.108312

Madenci, E., Ozkilic, Y.O., Hakamy, A. and Tounsi, A. (2023), "Experimental tensile test and micro-mechanic investigation on carbon nanotube reinforced carbon fiber composite beams", *Adv. Nano Res.*, **14**(5), 443-450. https://doi.org/10.12989/anr.2023.14.5.443

Mangalasseri, A.S., Mahesh, V., Mukunda, S., Mahesh, V., Ponnusami, S.A., Harursampath, D. and Tounsi, A. (2023), "Vibration based energy harvesting performance of magneto-electro-elastic beams reinforced with carbon nanotubes", *Adv. Nano Res.*, **14**(1), 27-43. https://doi.org/10.12989/anr.2023.14.1.027

Mehrabi, P., Honarbari, S., Rafiei, S., Jahandari, S. and Alizadeh Bidgoli, M. (2021), "Seismic response prediction of frc rectangular columns using intelligent fuzzy-based hybrid metaheuristic techniques", *J. Ambient Intell. Human. Comput.*, **12**, 10105-10123. https://doi.org/10.1007/s12652-020-02776-4

Mehrabi, P., Shariati, M., Kabirifar, K., Jarrah, M., Rasekh, H., Trung, N.T., Shariati, A. and Jahandari, S. (2021), "Effect of pumice powder and nano-clay on the strength and permeability of fiber-reinforced pervious concrete incorporating recycled concrete aggregate", *Constr. Build. Mater.*, **287**, 122652. https://doi.org/10.1016/j.conbuildmat.2021.122652

Mehrabi, P., Dackermann, U., Siddique, R. and Rashidi, M. (2024), "A review on the effect of synthetic fibres, including macro fibres, on the thermal behaviour of fibre-reinforced concrete", *Buildings*, **14**(12), 4006. https://doi.org/10.3390/buildings14124006

Mehrabi, P., Mortazavi, M. and Far, H. (2025), "Axisymmetric thermal post-buckling of the eccentric annular sector plate made of gori-metamaterials: introducing dnn-rf algorithm for solving the post-buckling problems", *Thin Wall. Struct.*, **208**, 112795. https://doi.org/10.1016/j.tws.2024.112795

Mirzaei, M. and Kiani, Y. (2016), "Free vibration of functionally graded carbon nanotube reinforced composite cylindrical panels", *Compos. Struct.*, **142**, 45-56. https://doi.org/10.1016/j.compstruct.2015.12.071

Moradi, H., Atashi, P., Amelirad, O., Yang, J.K., Chang, Y.Y. and Kamranifard, T. (2022), "Machine learning modeling and doe-assisted optimization in synthesis of nanosilica particles via stöber method", *Adv. Nano Res.*, **12**(4), 387. https://doi.org/10.12989/anr.2022.12.4.387

Mortazavi, B., Zhuang, X., Rabczuk, T. and Shapeev, A.V. (2023), "Atomistic modeling of the mechanical properties: the rise of machine learning interatomic potentials", *Mater. Horizons*, **10**(6), 1956-1968. https://doi.org/10.1039/D3MH00125C

Nazemizadeh, M., Bakhtiari-Nejad, F., Assadi, A. and Shahriari, B. (2020), "Nonlinear vibration of piezoelectric laminated nanobeams at higher modes based on nonlocal piezoelectric theory", *Acta Mechanica*. **231**, 4259-4274. https://doi.org/10.1007/s00707-020-02736-1

Reddy, J.N. (2003), *Mechanics of Laminated Composite Plates and Shells: Theory and Analysis*, CRC press.

Samaniego, E., Anitescu, C., Goswami, S., Nguyen-Thanh, V.M., Guo, H., Hamdia, K., Zhuang, X. and Rabczuk, T. (2020), "An energy approach to the solution of partial differential Eq.s in computational mechanics via machine learning: concepts, implementation and applications", *Comput. Meth. Appl. Mech. Eng.*, **362**, 112790. https://doi.org/10.1016/j.cma.2019.112790

Shu, J., Yu, H., Liu, G., Duan, Y., Hu, H. and Zhang, H. (2025), "DF-cdm: Conditional diffusion model with data fusion for structural dynamic response reconstruction", *Mech. Syst. Signal Pr.*, **222**, 111783. https://doi.org/10.1016/j.ymssp.2024.111783

Song, K., Yang, H., Liang, D., Chen, L. and Jaboyedoff, M. (2024), "Step-like displacement prediction and failure mechanism analysis of slow-moving reservoir landslide", *J. Hydrol.*, **628**, 130588. https://doi.org/10.1016/j.jhydrol.2023.130588

Song, X., Wang, W., Deng, Y., Su, Y., Jia, F., Zaheer, Q. and Long, X. (2024), "Data-driven modeling for residual velocity of projectile penetrating reinforced concrete slabs", *Eng. Struct.*, **306**, 117761. https://doi.org/10.1016/j.engstruct.2024.117761

Su, Y., Cui, Y.J., Dupla, J.C. and Canou, J. (2022), "Soil-water retention behaviour of fine/coarse soil mixture with varying coarse grain contents and fine soil dry densities", *Canadian Geotech. J.*, **59**(2), 291-299. https://doi.org/10.1139/cgj-2021-0054

Taheri, E., Firouzianhaji, A., Usefi, N., Mehrabi, P., Ronagh, H.

and Samali, B. (2019), "Investigation of a method for strengthening perforated cold-formed steel profiles under compression loads", *Appl. Sci.*, **9**(23), 5085. https://doi.org/10.3390/app9235085

Taheri, E., Firouzianhaji, A., Mehrabi, P., Vosough Hosseini, B. and Samali, B. (2020), "Experimental and numerical investigation of a method for strengthening cold-formed steel profiles in bending", *Appl. Sci.*, **10**(11), 3855. https://doi.org/10.3390/app10113855

Taheri, E., Mehrabi, P., Rafiei, S. and Samali, B. (2021), "Numerical evaluation of the upright columns with partial reinforcement along with the utilisation of neural networks with combining feature-selection method to predict the load and displacement", *Appl. Sci.*, **11**(22), 11056. https://doi.org/10.3390/app112211056

Toghroli, A., Mehrabi, P., Shariati, M., Trung, N.T., Jahandari, S. and Rasekh, H. (2020), "Evaluating the use of recycled concrete aggregate and pozzolanic additives in fiber-reinforced pervious concrete with industrial and recycled fibers", *Constr. Build. Mater.*, **252**, 118997. https://doi.org/10.1016/j.conbuildmat.2020.118997

Tounsi, A., Belabed, Z., Bounouara, F., Balubaid, M., Mahmoud, S., Bousahla, A.A. and Tounsi, A. (2024), "A finite element approach for forced dynamical responses of porous fg nanocomposite beams resting on viscoelastic foundations", *Int. J. Struct. Stabil. Dyn.*, 2650078. https://doi.org/10.1142/S0219455426500781

Wang, Y., Han, Z., Xu, X. and Luo, Y. (2024), "Topology optimization of active tensegrity structures", *Comput. Struct.*, **305**, 107513. https://doi.org/10.1016/j.compstruc.2024.107513

Wang, Z., Wang, K., Han, Q., Ni, J. and Wu, Z. (2025), "Crack imaging of underwater concrete components using interfacial waves and transducer array", *Mech. Syst. Signal Pr.*, **224**, 111998. https://doi.org/10.1016/j.ymssp.2024.111998

Wu, J., Yang, Y., Mehrabi, P. and Nasr, E.A. (2023), "Efficient machine-learning algorithm applied to predict the transient shock reaction of the elastic structure partially rested on the viscoelastic substrate", *Mech. Adv. Mater. Struct.*, 1-25. https://doi.org/10.1080/15376494.2023.2183289

Wu, Y., Li, Y., Yuan, H., Zhang, R., Jiang, Y., Liang, C., Zhu, Z., Liang, C. and Wang, X. (2024), "Efficient multi-objective coil design with deep neural network-accelerated pso in wpt systems", *Proceedings of the 2024 IEEE Transportation Electrification Conference and Expo*, Asia-Pacific (ITEC Asia-Pacific), IEEE, 956-961.

Xia, L., Wang, R., Chen, G., Asemi, K. and Tounsi, A. (2023), "The finite element method for dynamics of fg porous truncated conical panels reinforced with graphene platelets based on the 3-d elasticity", *Adv. Nano Res.*, **14**(4), 375-389. https://doi.org/10.12989/anr.2023.14.4.375

Xu, G., Guo, T., Li, A. qun, Zhou, T. and Shuang, C. (2025), "Seismic performance of steel frame structures with novel self-centering beams: shaking-table tests and numerical analysis", *J. Struct. Eng.*, **151**(3), 04025002. https://doi.org/10.1061/JSENDH.STENG-13516

Yang, H., Chen, C., Ni, J. and Karekal, S. (2023), "A hyperspectral evaluation approach for quantifying salt-induced weathering of sandstone", *Sci. Total Environ.*, **885**, 163886. https://doi.org/10.1016/j.scitotenv.2023.163886

Yang, H., Song, K., Chen, L. and Qu, L. (2023), "Hysteresis effect and seasonal step-like creep deformation of the jiuxianping landslide in the three gorges reservoir region", *Eng. Geol.*, **317**, 107089. https://doi.org/10.1016/j.enggeo.2023.107089

Yang, H., Qu, L., Chen, L., Song, K., Yang, Y. and Liang, Z. (2024), "Potential sliding zone recognition method for the slow-moving landslide based on the hurst exponent", *J. Rock Mech. Geotech. Eng.*, **16**(10), 4105-4124. https://doi.org/10.1016/j.jrmge.2023.08.007

Yang, H., Huang, G., Chen, C., Yang, Y., Wang, Q. and Dai, X. (2024), "Method for evaluation of geological strength index of carbonate cliff rocks: coupled hyperspectral-digital borehole image technique", *J. Rock Mech. Geotech. Eng.*, **16**(10), 4204-4215. https://doi.org/10.1016/j.jrmge.2024.08.013

Yang, L., Gao, Y., Chen, H., Jiao, H., Dong, M., Bier, T.A. and Kim, M. (2024), "Three-dimensional concrete printing technology from a rheology perspective: A review", *Adv. Cement Res.*, **36**(12), 567-586. https://doi.org/10.1680/jadcr.23.00205

Yang, Q., Li, H., Zhang, L., Guo, K. and Li, K. (2024), "Nonlinear flutter in a wind-excited double-deck truss girder bridge: experimental investigation and modeling approach", *Nonlinear Dyn.*, 1-19. https://doi.org/10.1007/s11071-024-10496-z

Ye, W., Shi, Y., Zhou, Q., Xie, M., Wang, H., Bou-Saïd, B. and Liu, W. (2024), "Recent advances in self-lubricating metal matrix nanocomposites reinforced by carbonous materials: a review", *Nano Mater. Sci.*, **6**(6), 701-713. https://doi.org/10.1016/j.nanoms.2024.02.007

Youzera, H., Meftah, S.A., Tounsi, A., Salem, M.A., Khedher, K. M. and Yaylacı, M. (2025), "Free vibration analysis of sandwich cylindrical shells with functionally graded carbon nanotube-reinforced composite face sheets using the differential quadrature (dq) method", *Acta Mechanica*. 1-16. https://doi.org/10.1007/s00707-025-04230-y

Zerrouki, R., Karas, A. and Zidour, M. (2020), "Critical buckling analyses of nonlinear fg-cnt reinforced nano-composite beam", *Adv. Nano Res.*, **9**(3), 211-220. https://doi.org/10.12989/anr.2020.9.3.211

Zerrouki, R., Zidour, M., Tounsi, A., Tounsi, A., Belabed, Z., Bousahla, A.A., Salem, M.A. and Khedher, K.M. (2024), "Buckling behavior of nonlinear fg-cnt reinforced nanocomposite beam reposed on winkler/pasternak foundation", *Comput. Concr.*, **34**(3), 297. https://doi.org/10.12989/cac.2024.34.3.297

Zhang, C., Duan, C. and Sun, L. (2024), "Inter-storey isolation versus base isolation using friction pendulum systems", *Int. J. Struct. Stabil. Dyn.*, **24**(2), 2450022. https://doi.org/10.1142/S0219455424500226

Zhang, W., Liu, X., Huang, Y. and Tong, M.N. (2022), "Reliability-based analysis of the flexural strength of concrete beams reinforced with hybrid bfrp and steel rebars", *Arch. Civil Mech. Eng.*, **22**(4), 171. https://doi.org/10.1007/s43452-022-00493-7

Zhang, Y.W., Ding, H.X., She, G.L. and Tounsi, A. (2023), "Wave propagation of cntrc beams resting on elastic foundation based on various higher-order beam theories", *Geomech. Eng.*, **33**(4), 381-391. https://doi.org/10.12989/gae.2023.33.4.381

Zhong, Y., Yu, R., Zhou, K. and Zhang, Z. (2025), "Parameter optimisation of piezoelectric vibration absorber in composite cylindrical shells: a multi-modal approach to mitigate stochastic vibration", *Thin Wall. Struct.*, **207**, 112713. https://doi.org/10.1016/j.tws.2024.112713

Zhou, X., Lu, D., Zhang, Y., Du, X. and Rabczuk, T. (2022), "An open-source unconstrained stress updating algorithm for the modified cam-clay model", *Comput. Meth. Appl. Mech. Eng.*, **390**, 114356. https://doi.org/10.1016/j.cma.2021.114356

Zhuang, X., Guo, H., Alajlan, N., Zhu, H. and Rabczuk, T. (2021), "Deep autoencoder based energy method for the bending, vibration, and buckling analysis of kirchhoff plates with transfer learning", *Eur. J. Mech. A Solids*, **87**, 104225. https://doi.org/10.1016/j.euromechsol.2021.104225

CC